Structures 80 (2025) 110027

Contents lists available at ScienceDirect

Structures

journal homepage: www.elsevier.com/locate/structures

Discontinuum rocking of rigid masonry macro-blocks using physics engines: analytical, numerical and experimental benchmarking

E. Giordano [a], Y. Han [a], A. Wang [a], G. Destro Bisol [a], S. Andrews [b], D. Malomo [a,*]

[a] Department of Civil Engineering, McGill University, 817 Sherbrooke Street West, Montréal H3A 0C3, Canada
[b] Department of Software and IT Engineering, École de Technologie Supérieure (ÉTS), 1100 Notre-Dame Street West, Montréal H3C 1K3, Canada

ARTICLE INFO

Keywords:
Rocking
Rigid body dynamics
Unreinforced masonry
Discontinuum analysis
Discrete models
Physics engines
Distinct Element Method

ABSTRACT

Rigid block rocking, significant across disciplines from structural to mechanical engineering, remains challenging to predict accurately using continuum-based numerical solutions. Traditional discontinuum simulation methods, although widely employed for modelling particle separation, re-contact, and collision with multiple contact points, often involve prohibitive computational cost. Analytical solutions, while computationally simpler, are limited primarily to straightforward planar cases with regular geometries. Physics engines - simulation platforms initially developed for digital animations and videogames - present an underexplored yet promising alternative for rigorously modelling multi-body rocking mechanics. These engines utilize discontinuum analysis principles comparable to established discrete models like the Distinct Element Method (DEM), but differ notably in contact detection and modelling strategies, typically providing faster, albeit less precise, predictions. This paper explores and enhances the capabilities of two physics engines - Bullet (integrated within Blender) and Vortex (within Vortex Studio) - to numerically simulate free and forced rocking of isolated and stacked rigid blocks, particularly from an earthquake engineering perspective. Rocking during seismic events frequently impacts blocky structural systems, such as unreinforced masonry (URM), posing assessment challenges for complex constructions. Initially, calibrated Bullet and Vortex simulations are compared with results from Housner's analytical equations for free rocking blocks with various aspect ratios. Subsequently, forced rocking responses to sine-pulse and sinusoidal base motions are examined, employing analytical solutions and referencing experimental and DEM-derived data across different frequencies and acceleration amplitudes. Lastly, the study replicates the rocking response of stacked blocks observed in shake-table tests using DEM, Bullet, and Vortex. Comparative analysis demonstrates that calibrated Bullet and Vortex models yield satisfactory accuracy while significantly reducing computational demands compared to conventional DEM approaches. Consequently, physics engines emerge as viable, efficient alternatives for simulating rocking mechanics, relevant both within structural engineering and beyond.

1. Introduction

The dynamic motion of rocking members is a relevant topic across multiple engineering domains, including structural, aerospace, and manufacturing engineering. Examples range from the design of vibration isolation systems in construction [22] to the delivery optimization of powder inhalers in pharmaceutical research or the study of spacecraft landers interacting with uneven surfaces [69]. In structural and earthquake engineering, rocking governs the mechanical response of a wide variety of building components, including, elevated water tanks, bridges piers, columns [80], chimneys, parapets and walls [28] – often idealized as rigid (at least in part). Since the pioneering work of Housner [35], several research studies have been conducted to uncover the mechanics of rocking (see e.g. [1,11,70]), now also widely used to design innovative low-damage dissipation devices (e.g. [71,40]). Predicting rocking motion is particularly important when assessing the seismic response of sub-standard (i.e. built before the modern standard codes) and old buildings, as those made of unreinforced masonry (URM), where the weak (or absent) connections among buildings constituents (e.g. floor-to-gable) often result in catastrophic rocking-governed collapses [75]. Advances in computer technologies and numerical modelling enabled in the last decades have allowed researchers to take advantage of the improved capabilities of a wide range of simulation tools, including the Finite Element Method (FEM). However, despite the

* Corresponding author.
E-mail address: daniele.malomo@mcgill.ca (D. Malomo).

https://doi.org/10.1016/j.istruc.2025.110027
Received 4 April 2025; Received in revised form 15 August 2025; Accepted 19 August 2025
Available online 1 September 2025

several successful applications available in literature [2,87], traditional continuum-based FEM are typically not suitable for simulating separation, contact and re-contact phenomena [26,73] characterizing rocking responses. For this reason, zero-thickness spring interfaces are often used to connect FE rocking members and surrounding environment (e.g. foundation, other rocking blocks), albeit at the cost of a high computational expense. The Distinct Element Method (DEM), originally developed to solve rock mechanics problems [16], has also been used to model rocking of URM [27] and reinforced concrete [72] members, mostly using rigid blocks and spring-based contact models. Despite the better adequacy of multi-contact DEM (i.e. those having multiple degrees of freedom per contact; Malomo and DeJong [51] demonstrated that at least 10 interface springs per rigid block are needed to effectively simulate URM rocking with DEM) codes and other discontinuum-based numerical techniques [43] to predict rocking mechanisms, the sometimes prohibitive analysis time presently prevents researchers from widely using it in real-world applications. In this paper, we investigate the applicability of a distinct family of discontinuum-based numerical approaches to URM rocking simulation, namely those typically used in the digital animation and robotics industries to create visually pleasing physical effects [3]. These physical engines [57] are capable of reproducing the mechanical interaction between solid bodies, albeit typically developed and calibrated to reproduce those in a simplified and effective fashion (i.e. efficiency over accuracy). Their use to solve engineering problems in a rigorous way, including those related to, e.g. geotechnics [33] and material design [39], has recently been scrutinized by various researchers, with positive results. Studies have also been performed on the collapse response of URM vaults using Project Chrono [9], as well as on the rocking response of URM columns under free and excited rocking impulses [49] via Blender. In this last contribution with Blender (widely used open-source modelling platform based on Bullet Physics), however, the authors could not find adequate match with analytical solutions for some of the geometries selected, which were also far from being applicable to URM analysis (e.g. they considered aspect ratios – i.e. height h over base b – ranging from 2 up to 8). In this paper, we focus on geometries (0.5–2.5 aspect ratios) compatible with the macro-block rocking simulation of URM members (e.g. walls, chimneys, parapets), improving previous modelling strategies. Our study also uncovers the adequacy of Bullet Physics engine simulations by comparing results against those predicted analytically through Housner's equations, numerically using Vortex (a distinct state-of-art commercial physics engine) and DEM, and measured experimentally via previous shake-table tests. This work is novel as it is the first 1) to investigate quantitatively and systematically the capabilities of physics engines against established numerical results and actual experimental data on rocking, 2) to consider a wide array of block sizes, shapes and boundary conditions, 3) to evaluate responses of rigid blocks under either free or forced rocking motions, 4) for both single and two stacked block systems. This work is relevant to computer scientists, mechanical and structural/earthquake engineers working on the rocking motion prediction of rigid blocks, either for improving the realism of animations or reducing the computational burden of rigorous mechanics-based evaluations. From a URM seismic response prediction standpoint, this paper offers first insights into a new family of simulation tools for expediting the rocking assessment of slender elements under base excitation, something that is presently rather impractical using traditional discontinuum modelling [72], and overambitious [42] if relying on analytical approaches alone.

2. Brief review of classic rigid block rocking analysis

In this section, an overview of the main assumptions and equations used in classic rocking analysis of rigid blocks is given. The methods described herein are later used to generate the analytical "ground truth" used for evaluating physics engines' predictions, in addition or in place of either experimental or numerical (DEM) results. In the classic analytical treatment of rocking mechanics for rigid particles, the equation of motion for a rectangular block with half-height h, half-width b, and mass m (Fig. 1.a), as proposed by Housner [35], relies on three key assumptions. First, the impacts are perfectly inelastic, meaning there is no bouncing. Second, the friction between the block and the foundation is sufficiently large to prevent any sliding. Third, the rocking motion is confined to a single plane. The geometric properties of rectangular blocks can also be described, as customary in the literature, by the radial distance from the center of rotation $R = \sqrt{h^2 + b^2}$, the critical (or slenderness) angle $\lambda = \tan^{-1}(b/h)$, and the mass moment of inertia $I_o = (4/3)mR^2$. When the horizontal ground motion $\ddot{u}_g$ exceeds the uplift acceleration $g\tan(\lambda)$, rocking motion is initiated (Fig. 1.c), and the block begins rotating with angle θ. The equation of motion of a rocking rigid block can be written as:

$$I_o\ddot{\theta} + mgR\sin[\mathrm{sgn}(\theta)\lambda - \theta] = -mgR\frac{\ddot{u}_g}{g}\cos[\mathrm{sgn}(\theta)\lambda - \theta] \quad (1)$$

where $p = \sqrt{3g/4R}$ is the frequency parameter of the block. In traditional analytical rocking dynamics, damping of the system is accounted for only through impacts as a reduction of angular velocity. The value of this reduction, η, is usually derived using the conservation of angular momentum principle before and after the impact about any corner [20]. Consequently, the post-impact angular velocity can be calculated based on the pre-impact velocity as follows, where the superscripts " and ' indicate the velocity after and before the impact, respectively:

$$\dot{\theta}'' = \eta\dot{\theta}' \quad \text{where} \quad \eta = 1 - \frac{3}{2}\sin^2\lambda \quad (2)$$

In this work, ordinary differential equation solvers (ODE45) in the MATLAB post-processing platform [81] were used to integrate the equations of motion for analytical formulations.

The previous model describes the rocking response of a single rigid block under dynamic excitation. In this work, a two-stacked rigid block system is also considered to evaluate the predictive capabilities of the physics engines. As in the single-block model, the geometry is defined by the height and width of each block, which determine their critical angle and radial distance from the pivot point. In addition to the critical angles of the lower block (λ_1) and the upper block (λ_2), and their respective radial distances (R_1 and R_2), a global slenderness parameter (λ), along with a corresponding radial distance (R), is introduced (Fig. 1.b). These represent the geometry of the system when it behaves monolithically as a single rigid block. Similarly, the rotation angles of the lower and upper blocks are denoted by θ_1 and θ_2 (Fig. 1.d), while the rotation angle corresponding to the rocking motion of the equivalent monolithic system is denoted by θ.

Compared to the single-block case, the two-block configuration introduces additional complexities in the dynamic behaviour: the system is characterized by two degrees of freedom, and the nonlinearity of the response increases significantly due to the presence of four distinct motion patterns. Transitions between these patterns can occur either through impacts or sudden changes in acceleration. For the sake of conciseness, the full formulation is not reported here; we refer the reader to the following works for further details [65,76,77,78].

Pattern changes due to acceleration are detected by equating the overturning (external) moments with the stabilizing (internal) moments, while impacts occur when the rotation of the lower body is zero or when the rotations of the two blocks are equal. Each impact is modelled using a coefficient of restitution, determined by applying the principle of conservation of angular momentum, similar to the single-block case. However, despite the conceptual similarity, the coefficient of restitution values for the two-block system can differ significantly. This is because impacts involve multiple bodies: for instance, the velocity of the upper block can increase following an impact between the lower block and the ground, hence a coefficient of restitution greater than one [22].

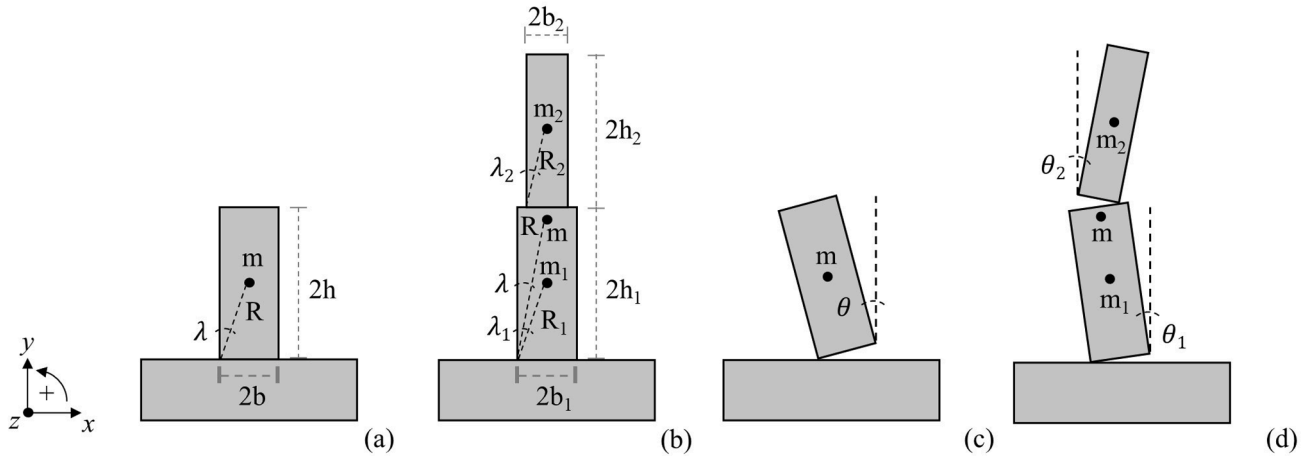

Fig. 1. Rigid rocking blocks models: single block system at rest (a) stacked blocks system at rest (b) single block system in motion (c) stacked blocks system in motion (d).

3. Discontinuum rocking mechanics of rigid blocks

Contact formulations used in physics engines share remarkable similarities with those typically implemented into rigorous discontinuum models used for rocking simulation of URM, while also featuring key differences allowing them to overcome the latter's traditional shortcomings. This section will comparatively discuss rigid body contact mechanics in physics engines and DEM, highlighting critical aspects in both numerical solutions that are particularly relevant for predicting the rocking motion of rigid blocks. Interested readers are referred to Malomo and Pulatsu [54] and Andrews et al. [3], from which the notation employed in the following sub-sections is taken, for further discussion on discontinuum methods and physics engines and their usual applications.

3.1. The Distinct Element Method

The DEM, originally formulated for the mechanical behaviour of particulate systems [18], simulates discrete bodies (rigid or deformable; in what follows, rigid block formulation alone is discussed) and their interactions at their boundaries through contact interfaces – determined through a contact (i.e., collision) detection process. Rigid blocks in DEM can be represented as polyhedral shapes with planar faces. Once two bodies are identified as "neighbours", the Common-Plane (CP) approach is used to confirm if the bodies are in contact, determine sub-contacts (i.e., contact points where joint constitutive relationships are applied), and establish their respective contact normal vector (i.e., the normal direction in the contact frame). This algorithm simplifies the number of possible collisions by (1) identifying a "common-plane" that bisects the space between two bodies and (2) testing each body individually for contact with the common-plane (i.e., effectively reducing the collision check to only vertex-plane interactions). Additional details about the CP formulation can be found in Cundall [17]. DEM, as implemented in 3DEC [36] typically used for URM and rocking simulations, see e.g. [55,68,52,59], uses a time-dependent incremental solution procedure, where the Newton equations of motion, $F = m\ddot{u}$, and Euler rotation equations, $M = I\dot{\omega} + \omega \times (I\omega)$, are solved for each mass point (m) and respective moment of inertia (I) using an explicit central difference method [32]. The displacement at sub-contact i over a time-step, Δt, can be expressed as $u_i^{t^+} = u_i^{t^-} + \dot{u}_i^{t^+}\Delta t$ and $\omega_i^{t^+} = \omega_i^{t^-} + \dot{\omega}_i^{t^+}\Delta t$ for translational and rotational displacements, respectively, where $t^+ = t + \Delta t/2$ and $t^- = t - \Delta t/2$. For conditional stability, DEM often uses an adaptive time-stepping scheme based on the Courant-Friedrichs-Lewy (CFL) condition such that $\Delta t \leq \Delta t_c = 0.2\sqrt{m_{\min}/k_{\max}}$, where Δt_c is the system's critical time-step, $m_{\min}$ is the minimum block mass and $k_{\max}$ the maximum contact stiffness [14].

The deformations at the joints (i.e., interface where contact points are established) are defined by constitutive laws, which in the case of dry-joints would feature zero tensile strength, $f_t = 0$, and infinite compressive strength, as well as a Mohr-Coulomb slip joint model in the shear direction (assuming zero cohesion c, zero dilatancy angle ψ, and equal initial and residual friction angles, ϕ). More complex interface laws are available for mortared contacts (see e.g. [66]), albeit not relevant for this study. The set of all possible shearing forces and their relationship with the contact normal stress can be visually represented using an isotropic friction cone as shown in Fig. 2. In the soft contact approach, the elastic stress increments, $\Delta\sigma_n$ (Eq.(3)) and $\Delta\tau_s$ (Eq.(4)), have a linear relationship with the relative point contact displacements, Δu_n and Δu_s (subscripts n and s denote normal and shear, respectively). This linear relationship is controlled using contact stiffnesses, k_n (normal) and k_s (shear), which introduces compliance (i.e., exceptional block interpenetration) between discrete bodies and adds numerical stability to the system. Contact stiffnesses can be computed using the physical properties of URM and other materials – such relationships and appropriate uses are thoroughly discussed in DeJong [19] and Malomo and Pulatsu [54].

$$\Delta\sigma_n = k_n \Delta u_n \tag{3}$$

$$\Delta\tau_s = k_s \Delta u_s \tag{4}$$

To model energy dissipation (i.e., from impacts or friction) in a dynamic system, 3DEC implements a local Rayleigh damping scheme with dashpot elements at the contact points. The resultant viscous damping forces and moments applied at contact point i can be expressed as $F_d = c\dot{u}_i^{t^-}$ and $M_d = c\dot{\omega}_i^{t^-}$, respectively, where c is the damping constant. Rayleigh damping combines mass and stiffness-proportional damping such that $c = \alpha m + \beta k$, where k is the contact stiffness (e.g., k_n or k_s) and α (Eq.(5)) and β (Eq.(6)) are the mass and stiffness-proportional damping constants, respectively [38]. DEM calculates the damping constants using two user-inputs: minimum critical damping ratio ($\zeta_{\min}$) and fundamental frequency ($f_{\min}$), where $f_{\min} = \omega_{\min}/2\pi$ ($\omega_{\min}$ is the fundamental angular frequency) [36]. Rocking mechanics of rigid blocks are sensitive to damping considerations, especially for undesired high-frequencies due to the "rattling effect" (i.e., high-frequency numerical noise) and rebound effects from impacts [27]. To mitigate these unwanted effects, DeJong [19] and Peña et al. [63] recommend stiffness proportional damping (i.e., $\alpha = 0$) for rocking behaviour. One can also approximate the critical frequency of a multi-block rocking system rather than calculating for all expected higher modes [19]. Procedures for selecting stiffness damping parameters (e.g., using an empirical

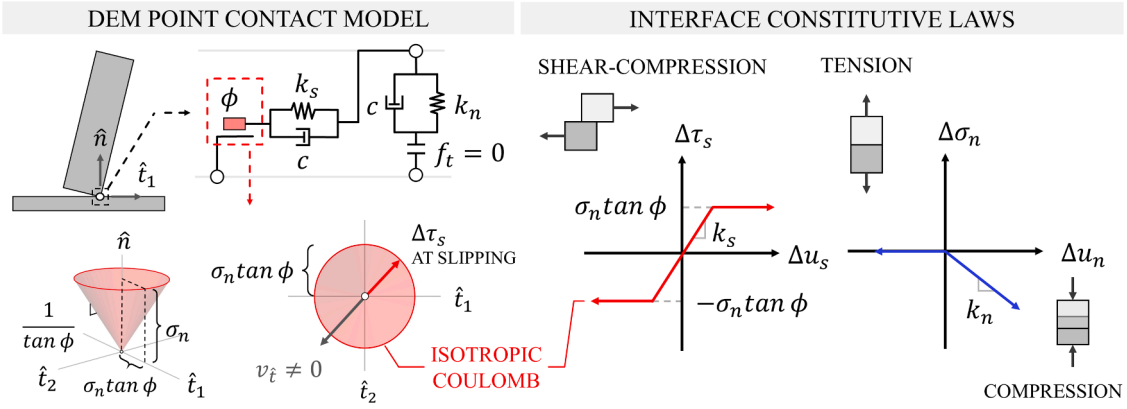

Fig. 2. DEM point contact model with isotropic Coulomb friction represented as a cone; interface constitutive laws in shear and normal directions – adapted from [3,84].

correlation between coefficient of restitution, e, and β) and approximating critical frequency for multi-block rocking systems are discussed therein.

$$\alpha = \zeta_{\min}\omega_{\min} \tag{5}$$

$$\beta = \frac{\zeta_{\min}}{\omega_{\min}} \tag{6}$$

Once the system forces are determined, the sub-contact translational ($\dot{u}_i$) and rotational ($\dot{\omega}_i$) velocities in Eq. (7) and Eq. (8) can be solved using time integration methods, where $\sum F_i^t$ and $\sum M_i^t$ represent the unbalanced forces and moments, respectively (i.e., sum of contact forces obtained from the stress increments, applied forces, and gravity loads). The displacements ($u_i^{t^+}$ and $\omega_i^{t^+}$) are then updated and the simulation proceeds to the next time-step. While a widely accepted form of modelling rocking behaviour for URM and other blocky systems, DEM often entails excessive computational times (up to 54 h for a free-rocking simulation with 15 sub-contacts, as demonstrated by Galvez et al. [27]) due to the various aspects discussed herein – e.g., stiffness proportional damping (requires smaller time-step) and additional sub-contacts (for a smoother transition between elastic to rocking phases).

$$\dot{u}_i^{t^+} = \dot{u}_i^{t^-} + \frac{\Delta t}{m}\left(\sum F_i^t - F_d\right) \tag{7}$$

$$\dot{\omega}_i^{t^+} = \dot{\omega}_i^{t^-} + \frac{\Delta t}{I}\left(\sum M_i^t - M_d\right) \tag{8}$$

3.2. Physics engines

Blender [58] is a 3D modelling tool that integrates the Bullet physics engine [13], and Vortex Dynamics [12] is a commercial physics engine developed especially for virtual reality training. Both engines model the rigid-body equations of motion using a velocity-level formulation of the dynamics and couple rigid bodies using kinematic constraints. Computational efficiency is a priority since these engines target real-time and interactive applications. Bullet uses an iterative numerical solver to compute constraint behaviour at each time step, whereas Vortex uses a specialized direct solver that is designed for engineering-grade accuracy. In more detail, Bullet uses sequential impulse and constraint-based solvers optimized for speed, suitable for real-time graphics with simplified contact resolution. In Bullet Physics, contact resolution typically uses a sequential impulse solver with hard constraints and low-accuracy approximations. It handles contact forces by iteratively solving constraint violations, usually converging within 10–20 solver iterations, which is sufficient for visual realism but introduces non-physical penetration or jitter in precise applications. Vortex uses a compliant contact model with constraint-based formulations, allowing for more physically accurate force and frictional responses. It supports sub-centimetre penetration tolerances and material-dependent stiffness and damping values. Simulations can be tuned to achieve convergence errors below 1 % in contact force magnitude, making its use in scenarios like soil-tool interaction or cable tension modelling (for which has been originally conceived) feasible. Readers can refer to the work of e.g. Izadi and Bezuijen [37] and Wagner [82] for further insights on solvers, contact and impact modelling within Bullet and Vortex, respectively. In what follows, an overview of the typical formulation common to both Bullet and Vortex is presented, alongside comparisons with DEM.

Bullet and Vortex follow a time-dependent incremental solution that is conceptually similar to that of DEM. Time discretization in computer graphics is commonly expressed in terms of frames per second, *FPS*, the rate at which the system can generate frames (i.e., proceed to the next time increment). This typically user-defined metric characterizes the visual quality of the simulation and is determined by the modelling application – e.g., faster (60–120 fps) for videogames and virtual reality applications, and slower (<30 fps) for 3D animations [10]. Physics engines will also reduce the time increment further for numerical stability by dividing each frame into n_s sub-steps [50], which are not always visually rendered but contribute to calculating the effective time-step, Δt, used in the time integration scheme (Eq. (9)). The respective time-step sizes for the aforementioned frame rates fall in the range of 0.008 – 0.04 s. Typical time-step for DEM range from $1e^{-9}$ to $1e^{-6}$ s [44], depending on the block size, stiffness, and density.

$$\Delta t = \frac{1}{(n_s + 1)(FPS)} \tag{9}$$

At each time-step, Δt, collision detection processes – necessary for separation and re-contact phenomena – are first implemented to identify objects that are in contact, defined as two bodies intersecting due to their collision shape. Collision shapes are used to approximate the volumes occupied by objects in space. Collision shapes for a body may be simplified from its actual geometry – spheres and boxes are popular for simplicity and efficiency [3]. However, convex hull (i.e., convex polygon that encloses a shape) approximations and mesh-based geometries are also used to capture finer details, albeit at a computational cost (more combinations of faces, vertices, and edges to check for intersections). The typical collision detection pipeline for physics engines occurs in two phases: (i) broad-phase and (ii) narrow-phase. Broad phase uses a simple shape (e.g., boxes) with computationally efficient collision tests to eliminate objects that are definitely not in contact [3]. This reduces the number of possible collisions that are then checked in the narrow-phase, which further refines the potential collisions using more complex geometries. Collision margins (buffers around the collision shape) can also be used to inflate collision shape sizes to catch

non-standard cases (e.g., edge-edge intersections). Finally, the objects that pass this test then proceed to narrow-phase collision detection in order to detect contact using the finest scale geometry in the simulation. Once colliding bodies are identified, the following key information is established: discrete contact points and their displacement in global space, $\boldsymbol{u}$, a contact normal direction to inform how bodies should move to avoid further inter-penetration, and a penetration (i.e., gap) measure, $\varphi(\boldsymbol{u})$, describing the distance between bodies (or distance that two bodies are intersecting).

While DEM typically uses explicit integration schemes to evaluate equations of motion (e.g., central difference algorithm) [15,43], semi-implicit time-stepping is preferred by physics engines for numerical stability as they favour larger (order of 10^{-2} s) time-steps. Some physics engines (e.g., Bullet) [13] will use semi-implicit methods as a compromise between numerical accuracy, speed, and stability; however, for ease of providing a simplified formulation and for appropriate, high-level conceptual comparisons with DEM, this discussion will focus on implicit techniques. Rigid body dynamics in physics engines are governed by Newton-Euler equations of motion [31], which take the form of a second-order ordinary differential equation (ODE) Eq.(10), where $\boldsymbol{M} \in \mathbb{R}^{n\times n}$ is the system masses, $\dot{\boldsymbol{u}} \in \mathbb{R}^n$ is the respective velocities, and $\boldsymbol{f}$ is the function that defines the applied forces on the system for each degree of freedom n. Note that rigid body computer graphics simulations typically operate at the velocity-level for computational efficiency and to ensure stable response to collision forces and impulses. The first-order Taylor expansion of the implicit velocities, $\dot{\boldsymbol{u}}^+ \approx \dot{\boldsymbol{u}} + \Delta t\ddot{\boldsymbol{u}}$ (the superscript + denotes implicit quantities), substituted into Eq.(10) yields a linear relationship for the kinematics of the rigid body system with respect to the chosen time-step, Δt (Eq.(11)).

$$\boldsymbol{M}\ddot{\boldsymbol{u}} = \boldsymbol{f} \tag{10}$$

$$\boldsymbol{M}\dot{\boldsymbol{u}}^+ = \boldsymbol{M}\dot{\boldsymbol{u}} + \Delta t\boldsymbol{f} \tag{11}$$

The kinematics of bodies in a simulation are limited through the application of constraints (e.g., boundary conditions, non-interpenetration requirements between bodies in contact). For a system with j constraints, the expression $\varphi(\boldsymbol{u}) \in \mathbb{R}^j$ is used to describe the "constraint manifold" (i.e., set of all possible rigid body motions that satisfy the given constraints at any given instant). Physics engines solve constraints in two groups: (1) bilateral constraints, $\varphi(\boldsymbol{u}) = 0$ (e.g., hinges, ball-and-socket joints), and (2) unilateral (i.e., contact) constraints, $\varphi(\boldsymbol{u}) \geq 0$ (e.g., objects cannot penetrate each other). The contact impulses needed to enforce these constraints are applied in a direction determined by the constraint gradient, $\boldsymbol{J} \in \mathbb{R}^{j\times n}$ Eq. (12), which is assumed to be constant throughout the time-step.

$$\boldsymbol{J} = \frac{\partial\varphi(\boldsymbol{u})}{\partial\boldsymbol{u}} \tag{12}$$

The normal contact impulse, $I_{\hat{n}}^+$ can be defined using a "push-only" spring-dashpot generated at the contact point – this behaves as a correctional impulse for interpenetration (with added numerical stability) and also allows the user more control over how strictly the constraints are solved (i.e., a tolerance for constraint enforcement). Note that bolded notation, $\boldsymbol{I}_{\hat{n}}^+$, represents the constraint impulse, whereas the not bolded notation, $I_{\hat{n}}^+$, represents the equivalent constraint force such that $\boldsymbol{I}_{\hat{n}}^+ = I_{\hat{n}}^+\Delta t$. While the spring does add potential energy to the system, it is paired with a damper to attenuate the response and prevent unrealistic collisions (e.g., "explosions"). The addition of this component, known as Baumgarte stabilization [8], yields a constitutive law that is mechanically analogous to the DEM point contact model in the normal direction. However, the spring-dashpot constraint equation takes the velocity dependent form $I_{\hat{n}}^+ = -k_n\varphi^+ - cv_{\hat{n}}{}^+$, where k_n and c are the contact stiffness and damping coefficients and $\varphi^+ = \varphi + \Delta t v_{\hat{n}}{}^+ = \Delta u_{\hat{n}}{}^+$ is the first order Taylor expansion approximated constraint error term (i.e., the relative displacement in the contact normal direction, $\Delta u_{\hat{n}}{}^+$), and $v_{\hat{n}}$ is the relative velocity in the contact normal direction. Rather than choosing k_n and c based on material and mechanical properties, these parameters can be determined depending on the desired level of constraint stabilization (i.e., how "strictly" the engine adheres to prescribed constraints and the effect of this on numerical stability). The relationship between these values is discussed later in this section. The resulting contact model (Fig. 3) is an intuitive linear relationship (valid for dry-joints; more complex contact laws do exist, e.g. bonded particles, see e.g. [25]): a greater contact impulse is required to prevent further overlap if the bodies are expected to continue penetrating in the next time step (i.e., $v_{\hat{n}}{}^+ < 0$), and a smaller or zero-magnitude impulse is applied if the bodies are in constant contact (i.e., $v_{\hat{n}}{}^+ = 0$) or moving away from each other (i.e., $v_{\hat{n}}{}^+ > 0$). No contact normal impulse is applied if the bodies are not in contact (i.e., zero tensile strength, $f_t = 0$). As in DEM, infinite compressive strength is herein assumed.

The shear component of the contact (i.e., constraint) impulse is determined through the implementation of the engine's chosen friction model – commonly Coulomb friction for its representation of planar dry friction and isotropic form [3]. The exact tangential contact impulse is bound by the inequality, $\|\boldsymbol{I}_{\hat{t}}\| \leq \mu\|\boldsymbol{I}_{\hat{n}}\|$, which defines a quadratic cone (i.e., the "friction cone") (Fig. 3) where $\mu = \tan\phi$ is the coefficient of friction. In the case of slipping (i.e., sliding), the direction of the friction force is chosen in the opposite direction, assuming principles of maximum energy dissipation. However, the isotropic friction cone representation of the stick-slip phenomenon presents itself as a non-linear complementarity problem (NCP), leading to numerical challenges. Linearized forms of the friction cone – e.g., polyhedral cone approximation [4,79], box approximation [41] – will discretize the envelope of possible friction forces into a discrete number of unit vectors. The tangential impulses, $\boldsymbol{I}_{\hat{t}}$, can be resolved into components with directions defined by the unit vectors. The respective magnitudes of the impulses in each direction are subsequently capped at $\mu\|\boldsymbol{I}_{\hat{n}}\|$ if needed. More unit vectors (e.g., a polyhedral with more sides) will typically yield a more exact solution but at a higher computational cost.

Once contact (i.e., constraint) forces are established, Eq.(11) is rewritten as the multibody system equation, Eq.(13), which includes the terms ϵ_j and υ_j representing the constraint force mixing (CFM) and error reduction parameter (ERP) for each constraint j, respectively. The ERP defines the portion of the constraint error, $\varphi^+ = \Delta u_{\hat{n}}{}^+$, that is resolved in the next time-step, while the CFM introduces artificial compliance to the system (i.e., allowing a tolerance for constraint violation). These constraint stabilization parameters are derived from the non-interpenetrative impulse, $I_{\hat{n}}$, and therefore can be tuned using Δt, k_n, and c. They also behave as feedback terms to reduce positional errors in the normal direction and improve the conditioning of the matrix in Eq. (13), improving stability – critical for real-time simulations. The coefficient of restitution, e_j, (typically 0) is also incorporated into the right-hand side of Eq.(13) – this parameter is introduced when setting up the constraint equations and determines the fraction of the initial velocity ($\dot{u}$) that was lost due to impact. It is also noted that Eq.(13) does not show additional parameters that are present if the friction cone is linearized (e.g., slack and auxiliary variables).

$$\begin{bmatrix} \boldsymbol{M} & -\boldsymbol{J}^T \\ \boldsymbol{J} & \boldsymbol{\Sigma} \end{bmatrix}\begin{bmatrix} \dot{\boldsymbol{u}}^+ \\ \boldsymbol{I}^+ \end{bmatrix} = \begin{bmatrix} \boldsymbol{M}\dot{\boldsymbol{u}} + \Delta t\boldsymbol{f} \\ -\boldsymbol{\Upsilon}\dfrac{\boldsymbol{\varphi}}{\Delta t} - \mathbf{E}\boldsymbol{J}\dot{\boldsymbol{u}} \end{bmatrix} \tag{13}$$

$$\boldsymbol{\Sigma} = \begin{bmatrix} \epsilon_1 & \cdots & 0 \\ \vdots & \ddots & \vdots \\ 0 & \cdots & \epsilon_j \end{bmatrix} \tag{14}$$

$$\boldsymbol{\Upsilon} = \begin{bmatrix} \upsilon_1 & \cdots & 0 \\ \vdots & \ddots & \vdots \\ 0 & \cdots & \upsilon_j \end{bmatrix} \tag{15}$$

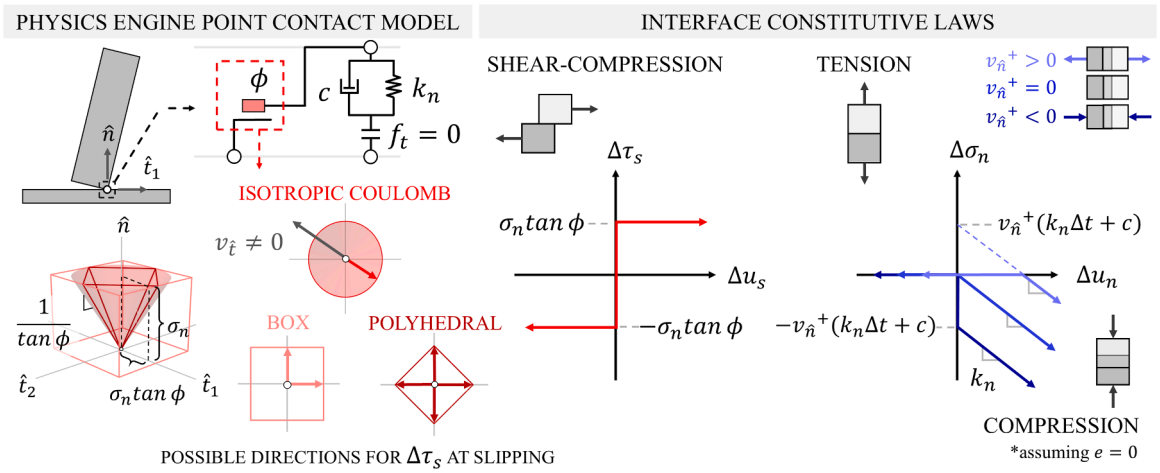

Fig. 3. Physics engine point contact model with friction cone approximations; interface constitutive laws in shear and normal directions expressed in the stress-displacement domain – adapted from [3,84].

$$\mathbf{E} = \begin{bmatrix} e_1 & \cdots & 0 \\ \vdots & \ddots & \vdots \\ 0 & \cdots & e_j \end{bmatrix} \tag{16}$$

To obtain the system velocities at the next time-step, $\dot{\boldsymbol{u}}^+$, physics engines employ constraint-based solvers to evaluate Eq.(13). It is noted that the complementarity conditions required to solve for unilateral constraints (e.g., friction impulses must lie within the "friction cone") are not shown in Eq.(13); however, the nature of these conditions (e.g., non-linear, linear, mixed linear) are considered in the choice of solver. These solvers can be generalized into three categories: (i) pivoting methods, which can find an exact solution using a direct solver (e.g., Lemke's Algorithm [47]), (ii) iterative methods, which find an approximate solution using iterations (e.g., Gauss-Seidel, Jacobi, Projected Gauss-Seidel [56,74]), and (iii) hybrid methods, which leverage advantages from both pivoting and iterative methods (e.g., Incremental Pivoting [7]). While iterative methods (their use well-established in DEM) are computationally expensive, introducing a cap on the number of solver iterations can expedite computations, albeit sacrificing numerical accuracy [24]. The updated rigid body displacements ($\boldsymbol{u}^+$) are found using the implicit approximation, $\boldsymbol{u}^+ = \boldsymbol{u} + \Delta t \boldsymbol{S} \dot{\boldsymbol{u}}^+$, where $\boldsymbol{S}$ maps the angular velocities in $\dot{\boldsymbol{u}}^+$ (solved using Eq.(13)) to their respective rigid body quaternion orientations.

4. Free rocking simulations for a single rigid block

This section examines the capabilities of Bullet and Vortex to simulate the free rocking behaviour of single rigid blocks. Before testing these engines with varying block slenderness and initial angles, sensitivity analyses were conducted to evaluate how different parameters inherent to the various codes employed might affect the results. The sensitivity analyses were conducted using a reference rigid block (hereinafter referred to as B0) with a rectangular base of 1 × 0.2 m^2, a height of 5 m, and a nominal mass of 1 kg. (although Eq.(1) shows that the rocking motion is independent of mass, most codes do require its specification). Gravity was set to −9.81 m/s^2 along the vertical y-axis, and the block was allowed to rotate freely from an initial rocking angle of 0.5 λ about the horizontal z-axis, where λ is the critical angle equal to 0.18 rad. Analyses were run for 20 seconds to ensure full energy dissipation and thus the end of the rocking motion. The initial parameters selected for running these preliminary analyses (whose results are compared to the analytical solutions in terms of rocking angle time-histories relative to λ; note that the monitored point is the block centroid) using Bullet and Vortex physics engines are summarized in Table 1.

Large values were chosen for solver iterations and sub-steps to ensure detailed and robust calculations at each time-step and accurately replicate the block's dynamic behaviour [49]. Regarding the collision shape, a box shape was selected as the simplest option that best fits the object's form. Translational damping, rotational damping, coefficient of restitution, and friction coefficients were chosen to align with Housner's assumptions [35]. In so doing, the models would only dissipate through opening/closing of discontinuities and friction (often referred to as physical damping [53]). With these initial (non-calibrated) settings and baseline model, the rocking responses shown in the graph in Fig. 4.a were obtained demonstrating good agreement between Bullet, Vortex and the analytical solution. The first eight seconds of motion predicted by both engines are virtually identical to their analytical counterpart; however, after that, Vortex exhibits a very slight phase shift. Bullet outcomes, on the other hand, continue to overlap until the end of the simulation, with only negligible differences – not readily noticeable. This phase lag in Vortex is believed to be linked to its use of integrators like backward Euler, which are known to suppress high-frequency dynamics and introduce random frequency shifts in oscillatory systems [34].

Table 1
Initial parameters considered in the baseline model for the free rocking sensitivity analysis of B0.

Parameter	*Unit*	*Bullet*	*Vortex*	*Analytical*
Solver iteration-steps	[step]	1000	1000	-
Collision shape	-	Box	Box	-
Collision margin	[m]	$1e^{-6}$	0.00	-
Simulation sub-steps	[steps/s]	200	200	-
Simulation rate	[fps]	240	240	-
Velocity damping	[Ns/m]	0.00	-	-
Coefficient of restitution	[%]	0.00	-	0.952
Friction coefficient	-	1.00	1.00	-
Friction angle	[°]	45	45	-
Translational damping	-	0.00	-	-
Rotational damping	-	0.00	-	-

Beyond the parameters set a priori to match Housner's assumptions in the baseline model, other critical ones (see Table 2) were varied to analyze their impact on simulation quality and efficiency. Bullet allows the modification of all these values, while Vortex only provides access to a few, as sub-steps and simulation rates. To perform the sensitivity analysis, two additional variations for each parameter were tested, as summarized below in Table 2. Effects on predictions were evaluated by individually changing each value, keeping others unaltered.

These additional sensitivity analysis results are summarized in Fig. 4. b-i. Overall, the initial rocking angles are well replicated in all cases,

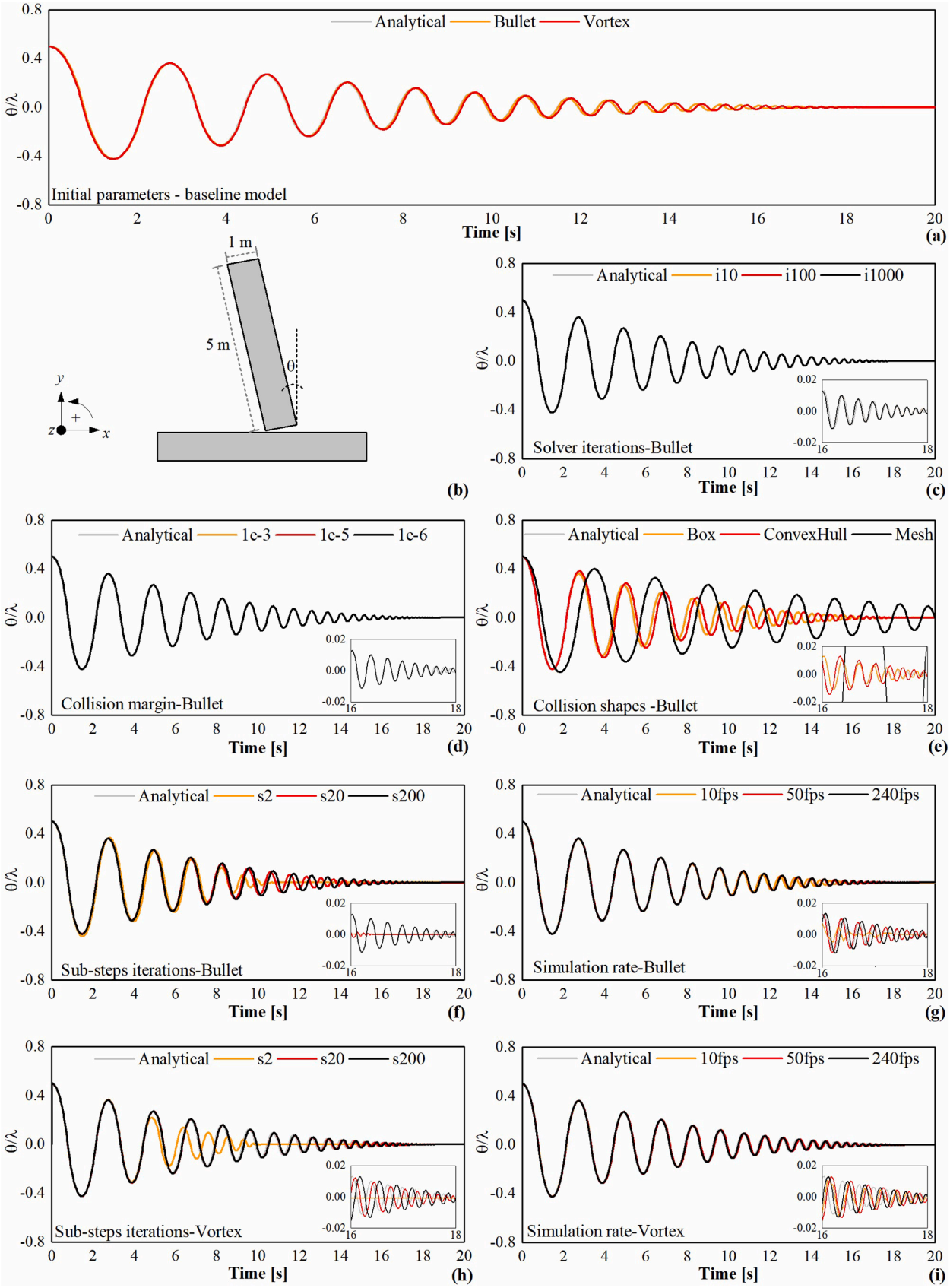

Fig. 4. Sensitivity analysis results for the reference block B0: Bullet and Vortex vs analytical solutions: normalized rocking angle time-histories.

Table 2
List of all parameters considered and tuned in the free rocking sensitivity analysis of the reference block B0.

Physics engine	*Parameter*	*Reference value*	*Values 1*	*Values 2*
Bullet	Solver iteration-steps [step]	1000	10	100
	Collision shape	Box	Convex Hull	Mesh
	Collision margin [m]	$1e^{-6}$	$1e^{-3}$	$1e^{-5}$
Bullet-Vortex	Simulation sub-steps [steps/s]	200	2	20
	Simulation rate [fps]	240	10	50

regardless of the changes applied, with the primary differences arising from the rate at which energy is dissipated due to impacts – hence later (i.e. after 2–5 s) in simulations. The largest deviation from analytical results occurs when Bullet's "mesh" collision shape is used, leading to significantly lower energy dissipation extent and rates. Conversely, using "convex hull" or "box" shapes produces results closer to Housner's curves, with the box shape providing the best match (Fig. 4.e). It is important to note that these collision shapes are not equivalent to the meshes used for geometry discretization in conventional numerical models. Instead, they are simplified volumetric approximations of the objects, which the software employs for contact detection (see Section 5). Users cannot directly specify their dimensions or characteristics, such as the mesh resolution in the "mesh" collision shape. The second most influential parameter affecting energy dissipation is the number of sub-step iterations. The best alignment with the analytical solution was achieved with 200 sub-steps, see Fig. 4.f and Fig. 4.h. With just 2 sub-steps, energy dissipated too quickly with both Bullet (11 s) and Vortex (10 s), a pattern that occurs when using up to 20 sub-steps in Bullet (17 s). The energy dissipation rate with 2 sub-steps is similar between Bullet and Vortex, with Vortex also showing a faster amplitude reduction. The simulation rate impacts only the final stages of motion, see Fig. 4.g and Fig. 4.i. With Bullet, Fig. 4.g, the best match with the analytical solution occurs with 50 fps. Using 10 fps produces a non-smooth time-history with premature motion stoppage, while 240 fps results in a delayed end-of-motion prediction. With Vortex, Fig. 4.i, 240 fps aligns best with the analytical solution, followed by 10 fps and 50 fps. Compared to Bullet, Vortex tends to dissipate energy more slowly at lower fps, with slight shifts in the final phase at each rate tested. With Bullet, the number of solver iterations, Fig. 4.c, and collision margin values, Fig. 4.d, had no significant effect on prediction accuracy. The variation of all the parameters had a negligible impact on the overall analysis time. The longest simulations, those run at 240 fps, required approximately 3.5 s to complete, whereas the slowest simulations, performed at 10 fps, took around 0.5 s. Having identified in the sensitivity exercise the most suitable parameters for the free rocking simulation of the reference block B0, these were tested on additional geometries, namely three different blocks (B1, B2, B3) with varying slenderness ratios (b/h). As the rocking motion is independent of mass, the default value of 1 kg set in the software was used for each block, consistent with the setup adopted for block B0. The response of these blocks was simulated using three different initial rocking angles, i.e. 20 %, 50 %, and 99 % of their respective critical ones (θ_{0_1}, θ_{0_2}, θ_{0_3}), see Table 3:

Fig. 5 shows that Bullet and Vortex results can satisfactorily match the analytical solutions, given that results almost overlap. Predictions differ slightly (order of magnitude is 10^{-4}) for B3 with initial rocking angle 0.2 λ, towards the end of the analysis. In this instance, the physics engines dissipated energy slower than the analytical model. This level of precision represents a substantial improvement over previous studies, such as Ma et al. [49], which reported discrepancies of up to 15 % in simulations of squat blocks.

5. Forced rocking simulations for a single rigid block

Having verified that the physics engines can satisfactorily approximate the free rocking response of single rigid blocks, herein both Bullet and Vortex models are tested under forced rocking. To this end, the experimental study by Peña et al. [62] was used as a reference to define the block dimensions and input characteristics. The abovementioned authors conducted rocking shake-table tests on single, stacked, and trilith granite blocks under free rocking, sinusoidal, and random motion. This section focuses on the block referred to as "Single # 2" (by the authors who have performed the experiments), with dimensions $0.17 \times 0.502 \times 1$ m^3 (Fig. 6.a) and a mass of 228 kg. The rigid block models were subjected to sine-pulses acceleration (Fig. 6.b, note this is a purely numerical exercise, as no experiments were actually performed using such an input) and sinusoidal acceleration excitations (Fig. 6.c). The rocking of the stacked blocks under sine-pulse excitation was performed to verify whether the differences observed in the single block's rocking response under sine-pulse were confirmed, and to analyze how the interactions between the top and bottom blocks were managed by the physics engines. Results were compared to analytical (Housner; both pulse and sinusoidal excitation), numerical (DEM; both pulse and sinusoidal excitation) and experimental results (sinusoidal excitation alone).

The frequencies (f) and amplitudes (A) used for the pulse-like and sinusoidal inputs are summarized in Table 4. Only a subset of those employed by Peña et al. [62] was considered—specifically, the frequency ($f=1/T$ where T is the period) and amplitude pairs that, according to analytical and experimental observation, generate accelerations sufficient to trigger the rocking mechanism (i.e. $\frac{\ddot{u}_g}{g\tan(\lambda)} = |1|$)

In 3DEC, the rigid block initially rested on a fictitious one with restrained rotations and uplifts representing the shake-table (hence modelled as a $1 \times 0.75 \times 0.25$ m^3 foundation plate), to which the shaking signals were applied in terms of velocity time histories, obtained by integrating the input acceleration. The parameters used for the rocking block and its interface with the foundation plate are summarized in Table 5 (with density ρ and friction angle ϕ taken from the experimental data available from [62]). To simulate dry-joint conditions, the properties of the joint interface between foundation and top rocking block, namely cohesion c, tensile strength f_t, and dilatancy angle ψ, were set to zero. Additionally, the normal and shear contact stiffnesses k_n and k_s were set to the minimum value ($1e^9$ N/m^3) required to prevent spurious block interpenetration (as suggested by [52]). To avoid unrealistic bouncing and excessive noises, a minimal amount (as no numerical damping was added into physics engine models) of Rayleigh damping proportional to stiffness alone (as opposed to its standard

Table 3
Additional geometries and initial rocking angles considered for the free rocking simulations of B1, B2, B3.

Block ID	*Height h*	*Base b*	*Thickness t*	*b/h*	λ	Initial rocking angles		
	(m)	*(m)*	*(m)*	(-)	*(rad)*	θ_{0_1} *[-]*	θ_{0_2} *[-]*	θ_{0_3} *[-]*
B1	0.75	0.50	0.20	0.67	0.59	0.20λ	0.50λ	0.99λ
B2	1.00	0.50	0.20	0.50	0.46	0.20λ	0.50λ	0.99λ
B3	1.25	0.50	0.20	0.40	0.38	0.20λ	0.50λ	0.99λ

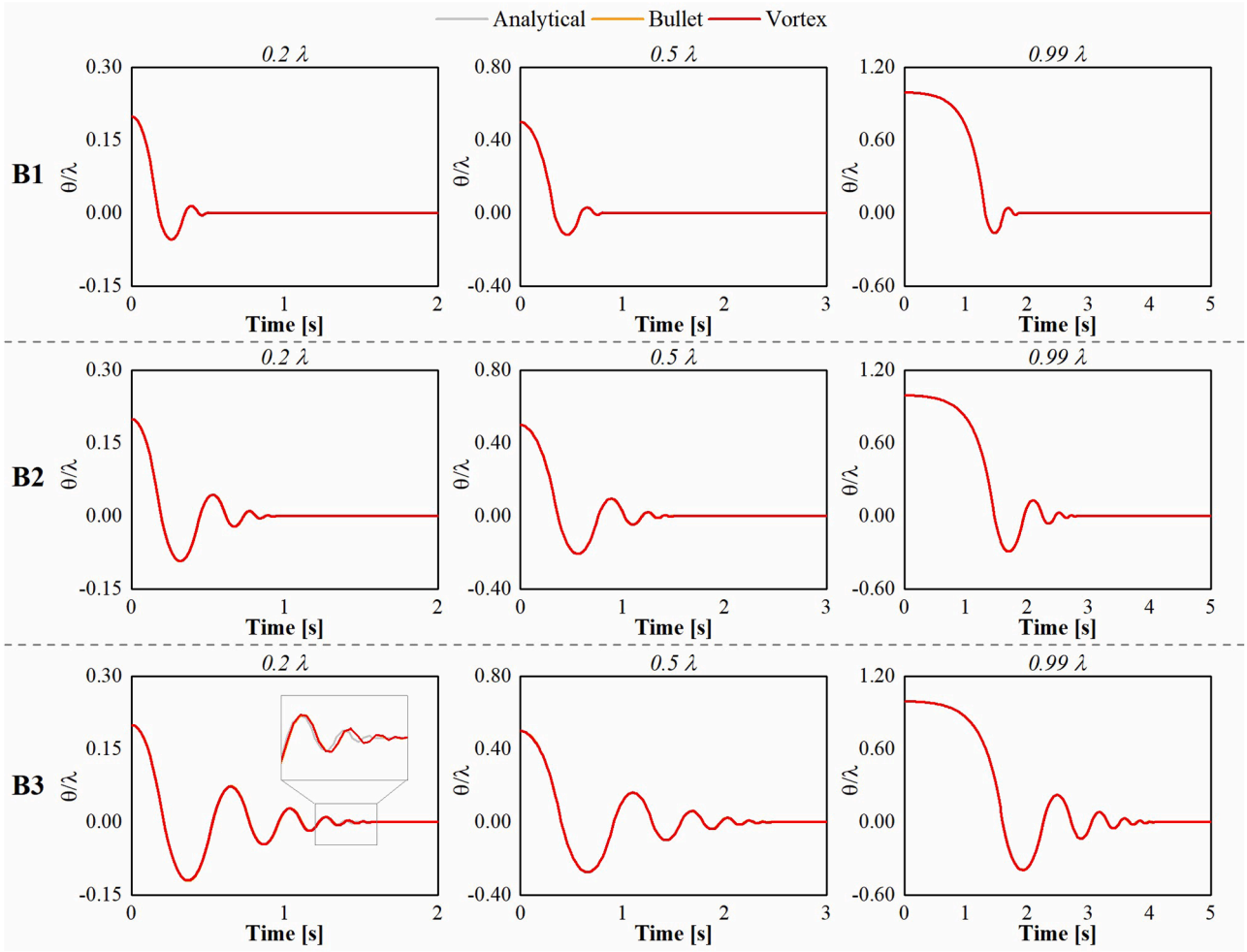

Fig. 5. Analytical vs physics engine models normalized free rocking angle time-histories for B1, B2, B3, starting from the three initial rocking angles 0.2 λ, 0.5 λ, 0.99 λ.

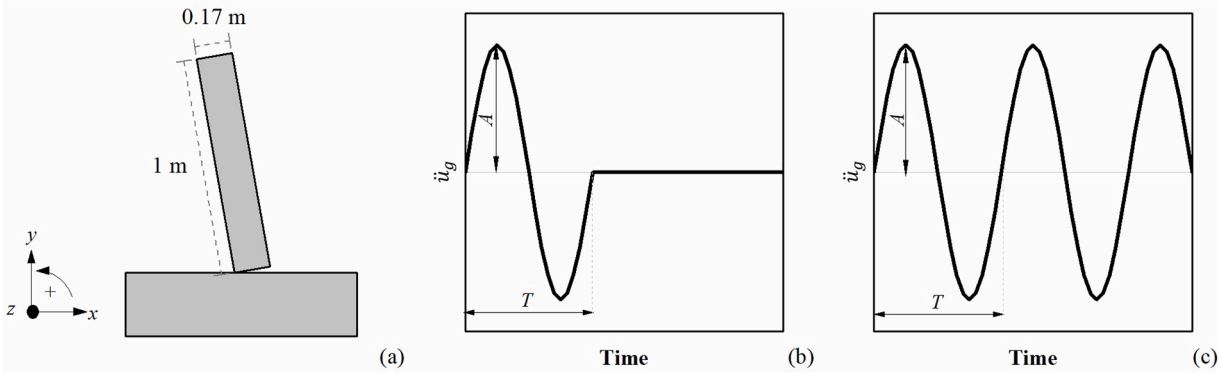

Fig. 6. Tested block's dimensions (a) and characteristics of the input considered for the forced rocking simulation: sine-pulse (b) and sinusoidal (c) excitations.

version, which includes considerations on mass too) was applied, following the procedure suggested by DeJong [19]. The critical frequency was selected based on the highest frequency in the system, which was determined from three types of impacts: edge impact w_e (surface in 3D), corner impact w_c (edge in 3D), and rotational impact w_r. The highest frequency identified was w_e, 1418 Hz, which corresponded to a constant damping factor, β, equal to 2.25×10^{-4}. Five sub-contacts were defined along the block thickness at the interface with the base, in order to achieve a smooth transition between elastic response and rocking [27]. This value is within the range suggested by several researchers [43,67], and was chosen as a compromise to ensure satisfactory results while maintaining reasonable computational time.

5.1. Response to sine-pulse excitations

The predicted rocking angle time-histories of the single rigid block under sine-pulse excitations are shown in Fig. 7. The upper section of the figure presents a complete time-history, while the lower sections zoom

Table 4
Summary of the characteristics considered derived by [62]'s experiments on "Single # 2".

Frequency f [Hz]	*Amplitude A* [mm]	$\ddot{u}_g$ [m/s^2]	$\frac{\ddot{u}_g}{g\tan(\lambda)}$ [-]
3	8	2.84	1.28
3.3	6	2.58	1.16
	8	3.44	1.54
5	4	3.95	1.77
	5	4.93	2.22
	6	5.92	2.66

Table 5
Parameters used in 3DEC to simulate the forced rocking experimental response of "Single # 2" [62].

ρ [kg/m^3]	k_n [N/m^3]	k_s [N/m^3]	ϕ [°]	c [N/m^2]	f_t [N/m^2]	ψ [°]	w_e [Hz]	β [-]
2670	$1e^9$	$1e^9$	45	0.0	0.0	0.0	1418	$2.25e^{-4}$

in on the first five seconds of each simulation to better highlight differences and similarities. The rocking oscillations obtained with Bullet, Vortex, and DEM are comparable in both magnitude and phase during the initial motion stages (until up to 1 s) for all frequency and amplitude combinations considered. In contrast, the analytical maximum angles differ slightly from those computed by the other programs. The largest discrepancy occurs with the sine pulse *5 Hz / 5 mm*, where the analytical maximum angle is 21 % higher than those obtained with both Vortex and DEM, and 25 % higher than that computed by Bullet. Vortex and DEM generally show larger rocking angles than Bullet (up to +5 %). Relative to the analytical solution, Vortex tends to overestimate rocking angles, while Bullet underestimates them, as illustrated by the comparison of the normalized maximum rotations with respect to the critical angle, λ, reported in Table 6. In the latter, θ_{an}, θ, θ_{vx} and θ_{DEM} stand for analytical, Bullet, Vortex and DEM block rocking angles taken at the block centroid. Both physics engines exhibit slightly overdamped behaviour compared to the analytical solution, while DEM shows a noticeably underdamped one. Moreover, results obtained with DEM, after the initial stages, show larger rocking angles and much longer oscillation periods compared to the other simulations.

Previous research on URM subjected to pulse-like base motions did reveal similar trends when comparing DEM analysis results of rocking [29] and arch [46] systems to analytical and different damping schemes, respectively. The stiffness proportional employed herein, although widely deemed as the most accurate option available for DEM [48], is also known for under-dissipating energy at impacts, as experienced by e. g. Galvez et al. [27].

The normalized maximum rocking angles, both analytical and numerical, are plotted against the corresponding normalized peak accelerations in Fig. 8. This type of plot is commonly used to investigate

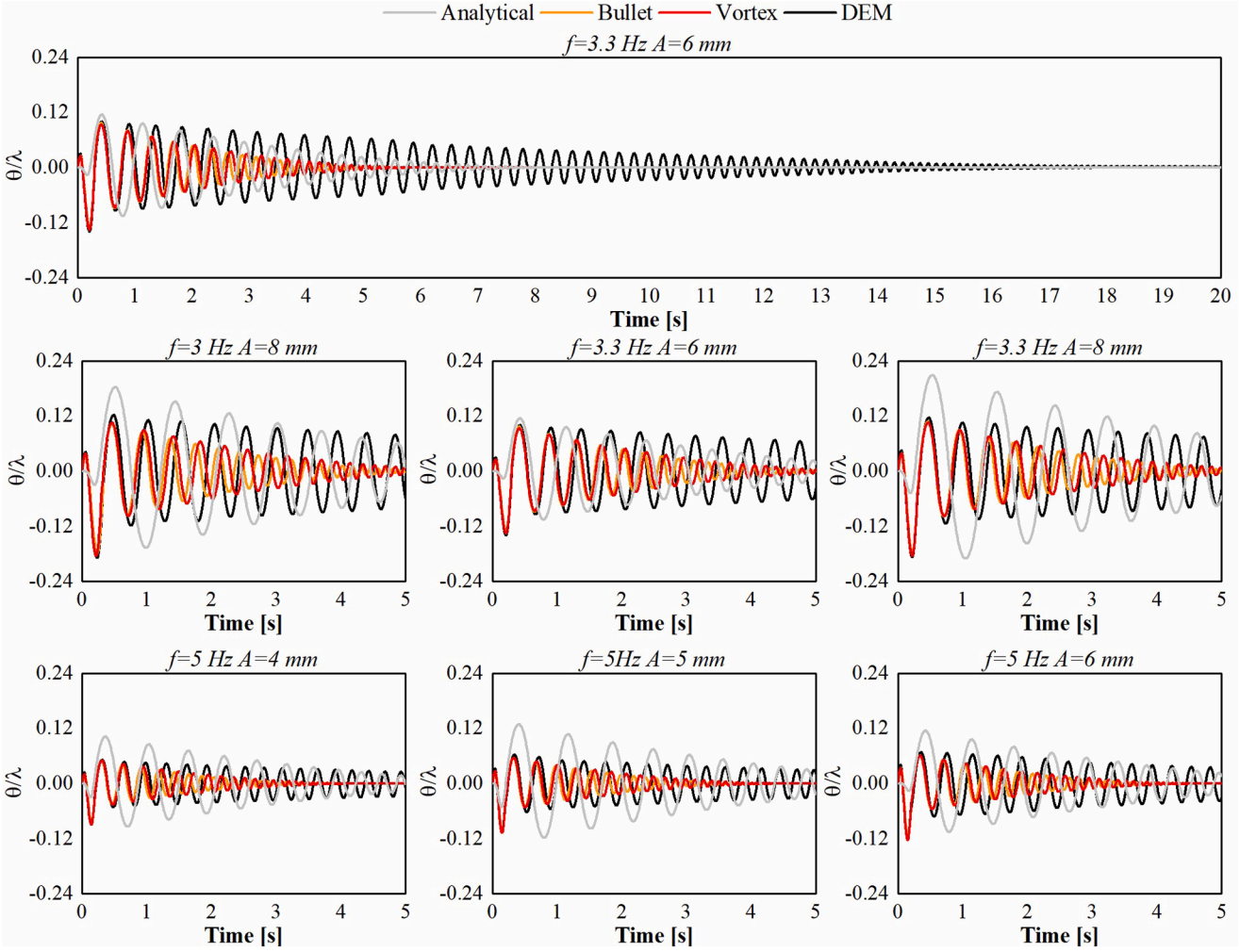

Fig. 7. Normalized rocking angle time-histories of the single block under sine-pulse excitations: comparison between Bullet, Vortex, DEM, and the analytical solution.

Table 6
Comparison of normalized maximum rocking angles obtained using analytical solutions, Bullet, Vortex and DEM, for a rigid block under sine-pulse excitation.

Frequency [Hz]	*Amplitude [mm]*	Analytical $\frac{\theta_{an}}{\lambda}$ [-]	*Bullet* $\frac{\theta_{bl}}{\lambda}$ [-]	*Vortex* $\frac{\theta_{vx}}{\lambda}$ [-]	*DEM* $\frac{\theta_{DEM}}{\lambda}$ [-]
3	8	0.183	0.179	0.184	0.189
3.3	6	0.115	0.130	0.135	0.139
	8	0.209	0.179	0.184	0.187
5	4	0.103	0.085	0.089	0.089
	5	0.129	0.103	0.107	0.107
	6	0.115	0.119	0.123	0.122

rocking behaviour, see as example the works of Papastamatiou and Psycharis [61] and Godio and Beyer [30]. The graph shows that, despite some discrepancies, all models and the analytical solution display a broadly similar rotational response to the imposed excitations. It also highlights that the rocking amplitude is more strongly influenced by the sine-pulse amplitude than by the peak acceleration. In fact, the largest rotations were recorded at normalized accelerations of 1.28 and 1.54, corresponding to input signals of *3 Hz / 8 mm* and *3.3 Hz / 8 mm*, respectively. In contrast, the smallest rotation occurred at a normalized acceleration of 1.77, corresponding to an input of *5 Hz / 4 mm*. Notably, *8 mm* and *4 mm* were the maximum and minimum amplitudes considered. This find confirm as what observed by other researchers like Yim et al. [85] that the rocking motion is sensitive to the characteristics of the ground motion

The maximum rocking angles derived from the analytical solution have magnitudes comparable to those obtained from the different codes used, as shown in Fig. 8, but they occur in the opposite direction. This difference becomes evident when examining the time-histories between 0 and 0.2 s (Fig. 9.a). In both DEM and physics engines, it is worth noting that the rocking motion is simulated by applying input loads (in terms of x-velocity in DEM, following common practice [45,60], and x-displacement in the physics engines, since these tools do not allow velocity or acceleration inputs) to the foundation plate when the system is at rest. This causes the block to rotate in the opposite direction of the input due to inertia (Fig. 9.b), a behaviour also observed by DeJong and Vibert [21] and by Zhang and Makris [86] in their studies on the response of a masonry spire and a rigid block, respectively, subjected to sine pulse ground acceleration. In contrast, the analytical formulation assumes that input forces (in terms of acceleration) are applied directly to the centroid of the block, which begins to move in the input direction (Fig. 9.c) once the activation acceleration threshold is reached (i.e. $\frac{\ddot{u}_g}{\text{gtan}(\lambda)} = |1|$). This intrinsic modelling difference explains the similar magnitude and opposite phases.

5.2. Response to sinusoidal excitations

The response of the block under sinusoidal excitations was analyzed in what follows using the same amplitude and frequency combinations chosen for the sine-pulse excitations, based on the experiments of Peña et al. [62] (Table 4). Maximum rocking angles obtained from the physics engines were compared with those from DEM, as well as with the analytical formulation and experimental shake-table tests. Generally, the block's motion under sinusoidal excitation features two distinct phases: transient and stationary, with maximum rocking angles occurring during the transient phase. Overall, for each of the base excitations considered, Bullet, Vortex, and the analytical solution predicted the transition between these phases at nearly the same moment in time, while DEM reached the stationary phase more slowly – similarly to what was observed in sub-Section 5.1. In the stationary phase, the rocking angles simulated in Bullet, Vortex, and DEM were closely aligned, while those computed analytically were slightly smaller. Fig. 10 shows the time-histories of the rocking angles for each input analyzed, with zooms between 0 and 2 s, start of motion, 8–10 s, section of the transient phase, and 53–55 s, section of the stationary phase. It should be noted that the full experimental motion of the block is not available for comparison. The only experimental data reported in the reference study are the maximum rocking angles, which values are shown in in Fig. 10 by dot dash lines.

In the first two seconds, the graphs illustrate that the rocking angles predicted by the analytical solution begin later than those from Bullet, Vortex, and DEM, similar to the observations for sine-pulse excitations. This delay is attributed to the direct application of acceleration to the block's centroid. However, the initial large rocking angles predicted by the analytical solution match in both magnitude and direction those predicted by all computational codes employed, with results from the physics engines and DEM being closely aligned during this transient phase. During the transient phase (8–10 s), the results from the different programs diverge, particularly under *3.3 Hz / 6 mm* and *5 Hz / 6 mm.* In the first case, DEM results show larger rocking angles, while in the second case, DEM and Vortex produce nearly identical responses. This response is characterized by a wobbling oscillation, similar to that observed by Tabbara et al. [80], where the block rotates not only around the z-axis but also around the y-axis when subjected to high-frequency, high-amplitude inputs. This suggests that Vortex, despite being a physics engine, is capable of capturing this complex three-dimensional behaviour similarly to 3DEC. However, under the *5 Hz / 6 mm* sinusoidal input, only DEM predicts the overturning of the top block between the transient and stationary phases, occurring at around 35 s. This collapse may be attributed to unrealistic numerical bouncing, likely triggered by an excitation frequency lower than the system's damped fundamental frequency. In the stationary phase, the rocking angles obtained with Bullet and Vortex are nearly identical, with DEM's results close to them. The analytical solution yields smaller amplitudes but similar periods. The only exception is the aforementioned one, *5 Hz / 6 mm*, where Vortex shows unstable but periodic rocking angles, while DEM records no rotations as the block had collapsed in the previous stage. Table 7 compares the maximum rocking angles obtained with each tool, where θ_{an}, θ_{bl}, θ_{vx} and θ_{DEM} stand for analytical, Bullet, Vortex and DEM blocks centroids rocking angles, against the experimental values, θ_{ex}. In general, the rocking angles predicted by the programs are close to the

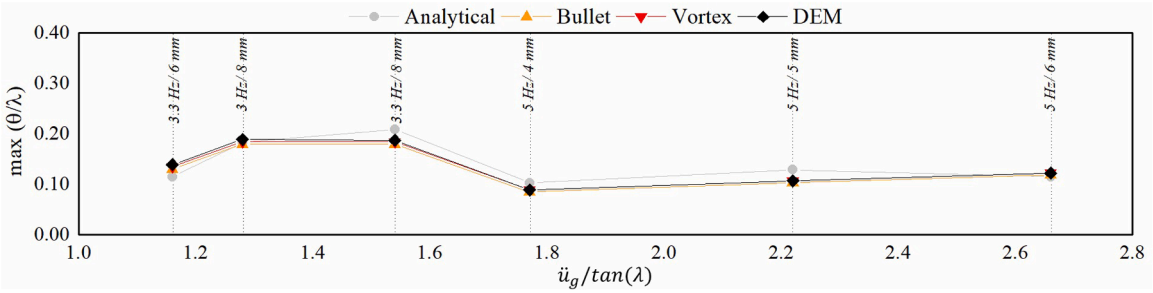

Fig. 8. Trends in the normalized maximum rocking angles of the 'single # 2' model under sine-pulse excitation, as a function of normalized input acceleration.

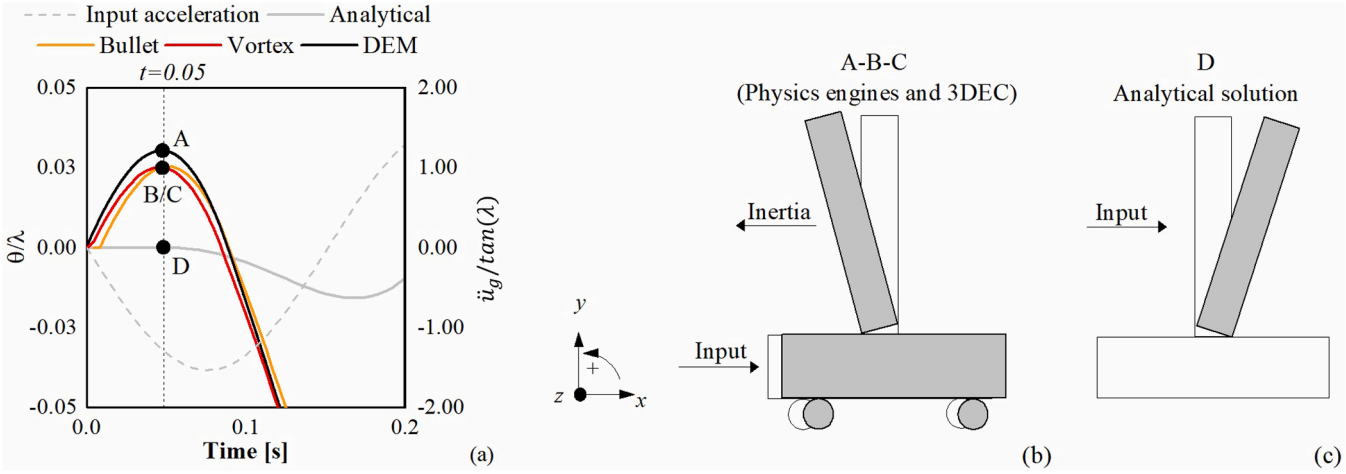

Fig. 9. Intrinsic differences in rocking modelling between physics engines, numerical and analytical solutions: a) rocking angles comparison at the motion start, b) graphical representation of the initial rocking angle direction in physics engines and DEM and c) graphical representation of the initial rocking angle direction in the analytical solution.

experimental results, with a maximum difference of 12 %. This excludes the results obtained with Vortex and DEM for the sinusoidal load at *5 Hz / 6 mm*. Overall, DEM provides the most accurate predictions of maximum rocking angles, followed by Vortex and Bullet, respectively. In contrast, the maximum rocking angles obtained analytically are consistently smaller than the experimental values, with differences ranging from 38 % to 43 %. It is interesting to note that under sinusoidal loads, DEM models did not yield overdamped results when compared to their physics engine counterparts. This phenomenon is explicable, as in this latter case blocks are continuously forced to move, as opposed to the pulse-like excitations where a "resting" phase was added to let the block ending its motion (Fig. 6.a). Also, sinusoidal motions tend to excite less numerical damping (since there is no sharp discontinuity in the signal).

The normalized maximum rocking angles of the single block under sinusoidal excitations, plotted against the corresponding normalized peak accelerations, confirm—similarly to the sine-pulse case—that the amplitude is the primary driver of the rotational response (Fig. 11). An exception to this trend occurs for the input of *5 Hz / 6 mm*, where Vortex shows significantly larger maximum rotations and the block collapses in the DEM simulation. As previously discussed, this anomalous response is likely due to the activation of a wobbling motion, which was not observed experimentally, nor predicted by the analytical solution or Bullet. The graph also highlights that, although the analytical solution underestimates the rocking amplitude, its trend with increasing acceleration closely follows that observed in the experiments and in Bullet simulations.

6. Forced rocking simulations for two stacked blocks

In this last section, the physics engines were tested using a system of two stacked blocks subjected to either sine-pulse or sinusoidal base excitations. Similarly to Section 7, results are compared against analytical results, obtained using available models from the literature [64] and Destro Bisol et al. [23], and DEM predictions for both the sine-pulse and sinusoidal signals (Table 8). Additionally, the experimental results from Peña et al. [62], in terms of maximum rotations, were also included for comparison with the response to sinusoidal excitation. As in the tests of Section 7 on the forced rocking of the single block, the dimensions and input parameters were herein also based on the experimental tests of Peña et al. [62]. The bottom block measures 0.20 × 0.4 × 0.60 m^3, while the top block measures 0.15 × 0.55 × 0.60 m^3. Both blocks had their corners cut 5 mm with a 45° angle to prevent their crashing during the rocking motion. This system is characterized by three critical angles, λ=18.45° for the bottom block, λ=14.04° for the top block and λ=9.85° for the whole system, assuming it behaves like a single block. The response of two stacked rocking blocks to sine-pulse ground motion can be assessed by considering the slenderest configuration between the top block and the monolithic system, as demonstrated in Destro Bisol et al. [22]. Accordingly, the smallest critical angle was used as a reference for normalizing the results. As for the single rigid block, only the amplitudes and frequencies combinations from Peña et al. [62] characterized by an acceleration, $\ddot{u}_g$, larger than the one evaluated with the critical angle ($\frac{\ddot{u}_g}{g\tan(\lambda)}$) were considered (see Table 8).

6.1. Response to sine-pulse excitations

Fig. 12 presents the normalized rocking angle time-histories obtained using sine-pulse excitations, divided between the top and bottom blocks at the start of the motion. Depicted results show that, under each input, the first two rocking angles produced by the physics engines and DEM are similar, particularly between DEM and Vortex. However, the analytical solution differs due to the inertia phenomenon described in Section 5.1.

The rocking response of the stacked blocks under sine pulse excitation can be characterized by non-harmonic motion dissipation, due to interactions between the top and bottom blocks. In such systems, it is possible for the blocks to move out of sync. When this occurs, energy is exchanged during impacts—specifically, when the top block collides with the bottom block while the latter is still in a rotated position—resulting in sudden changes in motion. In the analyzed cases, this behaviour is particularly evident for the sine inputs *4 Hz / 5 mm*, *5 Hz / 3 mm*, and *5 Hz / 4 mm*. The phenomenon is most prominent in the analytical and Bullet results but can also be observed, though less distinctly, in the Vortex and DEM results. The predicted maximum rocking angles of the blocks centroids normalized to the minimal critical angle λ, are summarized in Table 9 and Table 10, for the top and bottom block, respectively. Their trends, plotted against the normalized maximum acceleration, are shown in Fig. 13.

The top block exhibits larger rocking angles, with values of 0.572 rad, 0.273 rad, 0.234 rad, and 0.320 rad for the analytical solution, Bullet, Vortex, and DEM, respectively. These rocking angles occurred under different input conditions: *4.0 Hz / 5 mm* for the analytical solution and Bullet, *5.0 Hz / 4 mm* in Vortex and *3.3 Hz / 4 mm* in DEM. In contrast, the bottom block consistently showed small rocking angles that dissipated quickly. The maximum rocking angles reached were 0.021 rad for the analytical solution and Bullet, 0.008 rad for Vortex, and 0.015 rad for DEM. As with the top block, these values

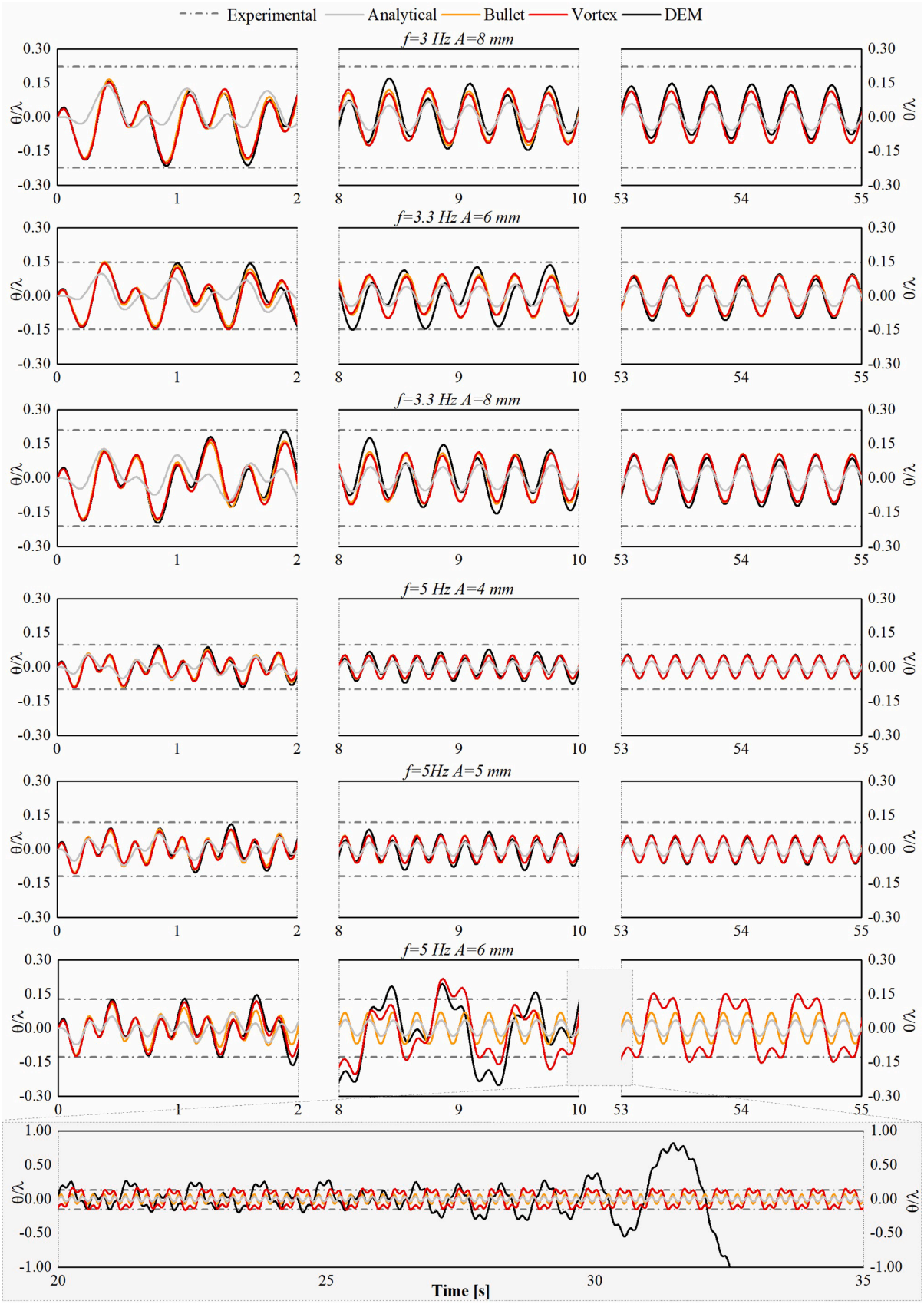

Fig. 10. Normalized rocking angle time-histories at the start of the motion, in the transitionary phase and the stationary phase of each combination of frequency and amplitude analyzed.

Table 7
Percentage errors in rocking angles for Bullet, Vortex and DEM, relative to experimental values for blocks under sinusoidal excitations (red indicates overestimations, blue underestimations vs experimental results).

Frequency [Hz]	*Amplitude* [mm]	Analytical $\frac{\theta_{an}-\theta_{ex}}{\theta_{ex}}$ [-]	Bullet $\frac{\theta_{bl}-\theta_{ex}}{\theta_{ex}}$ [-]	Vortex $\frac{\theta_{vx}-\theta_{ex}}{\theta_{ex}}$ [-]	DEM $\frac{\theta_{DEM}-\theta_{ex}}{\theta_{ex}}$ [-]
3	8	38 %	11 %	8 %	4 %
3.3	6	34 %	1 %	1 %	9 %
	8	39 %	11 %	12 %	2 %
	4	43 %	10 %	9 %	7 %
5	5	40 %	12 %	10 %	2 %
	6	43 %	7 %	107 %	collapsed

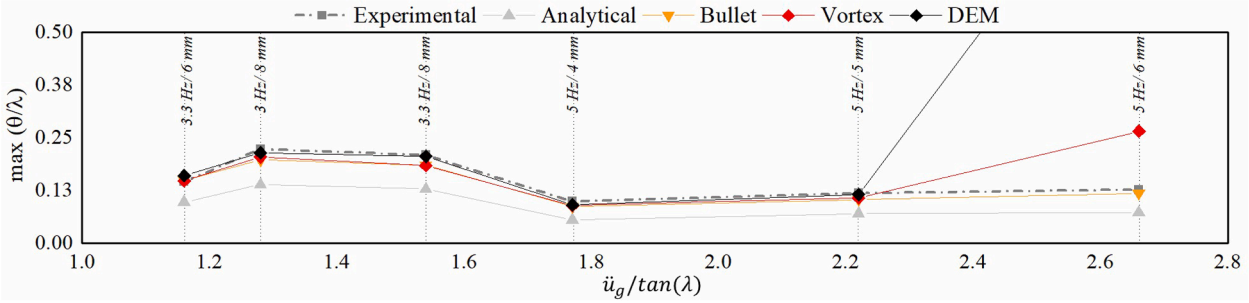

Fig. 11. Trends in the normalized maximum rocking angles of the 'single #2' model under sinusoidal excitation, as a function of normalized input acceleration.

correspond to different input conditions: *4.0 Hz / 5 mm* for the analytical solution, *4.0 Hz / 5 mm* and *5 Hz / 4 mm* for Bullet, *3.3 Hz / 4 mm* for Vortex, and *5 Hz / 4 mm* for DEM.

Fig. 13 shows, as for the single block, that an increase in acceleration does not necessarily lead to an increase in rocking angle for either the top or bottom block. In this system, both frequency and amplitude appear to significantly influence the rocking response. Specifically, for the *5 Hz* input, the rocking angle increased with amplitude up to *4 mm*, but then decreased for *5 mm*. This behaviour suggests that, during the half-cycle of the excitation, the block may not have reached its maximum rotation before the input reversed direction, causing it to rock in the opposite direction without completing the full excursion. The plots also indicate that, for the top block, the analytical solution predicts larger rotations than the numerical models for normalized accelerations greater than 1.72. In contrast, for the bottom block, this overestimation is evident in both the analytical solution and the Bullet model—although for the *5 Hz / 5 mm* input, all models appear to be in good agreement.

The rocking motion of the blocks dissipates over time, with the dissipation rate depending on the simulation tool used. DEM shows the slowest dissipation, with the blocks taking more than 10 s to come to rest, followed by Bullet (about 3 s) and Vortex (less than 2 s, see Fig. 12). The dissipation observed in the analytical solution is tends instead to be faster than in DEM, but it does not follow a consistent trend compared to Bullet and Vortex. For instance, under input conditions such as *4 Hz / 4 mm*, *4 Hz / 5 mm*, *5 Hz / 4 mm*, and *6.5 Hz / 2 mm*, the energy dissipates more slowly than in both physics' engines, while in other cases it is comparable to Vortex. This suggests that the interaction between the top and bottom blocks has a stronger influence on energy dissipation in the analytical solution than in the other numerical tools. The residual rotation shown by DEM under certain input conditions does not indicate that the block remained tilted, but rather that it experienced sliding. This sliding behaviour is specific to DEM, where contacts are modeled using normal and shear springs that can elastically deform up to a defined limit. In contrast, the physics engines employ non-smooth contact models, in which transitions between sticking and sliding occur instantaneously, without capturing the elastic deformation phase at the contact interface.

Table 8
Summary of the input characteristics used for the two stacked blocks forced rocking simulations.

Frequency [Hz]	*Amplitude* [mm]	$\ddot{u}_g$ [m/s^2]	$\frac{\ddot{u}_g}{g\tan(\lambda)}$ [-]
3.3	4	1.72	1.01
	3	1.90	1.11
4	4	2.53	1.48
	5	3.15	1.85
	2	1.97	1.16
5	3	2.96	1.74
	4	3.95	2.32
6.5	2	3.34	1.96

6.2. *Response to sinusoidal excitations*

The normalized rocking angle time-histories of the two stacked blocks under sinusoidal excitation are shown in Fig. 14, where analytical and numerical maximum rocking angles are compared against experimental values from Peña et al. [62] (the full experimental motion of the block is not available for comparison. The only experimental data reported in the reference study are the maximum rocking angles). Since maximum rocking angles typically occur in the initial stages, only the first two seconds are reported.

Table 11 and Table 12 summarize the percentage differences between the maximum rocking angles obtained analytically and numerically with respect to the experimental data for both the top and bottom blocks. Overall, the top block rocking angles are better simulated than those of the bottom block, likely due to the smaller rotation values in the latter.

For the top block, the rocking angles amplitudes obtained are generally lower than those reported by Peña et al. [62]. The results from DEM best approximate the experimental data, with percentage differences between 0 % and −43 %, and also successfully simulate collapses at *4.0 Hz / 5 mm* and *5.0 Hz / 4 mm*, which occur at approximately 4.65 s and 5.22 s, respectively (see miniatures in Fig. 11). However,

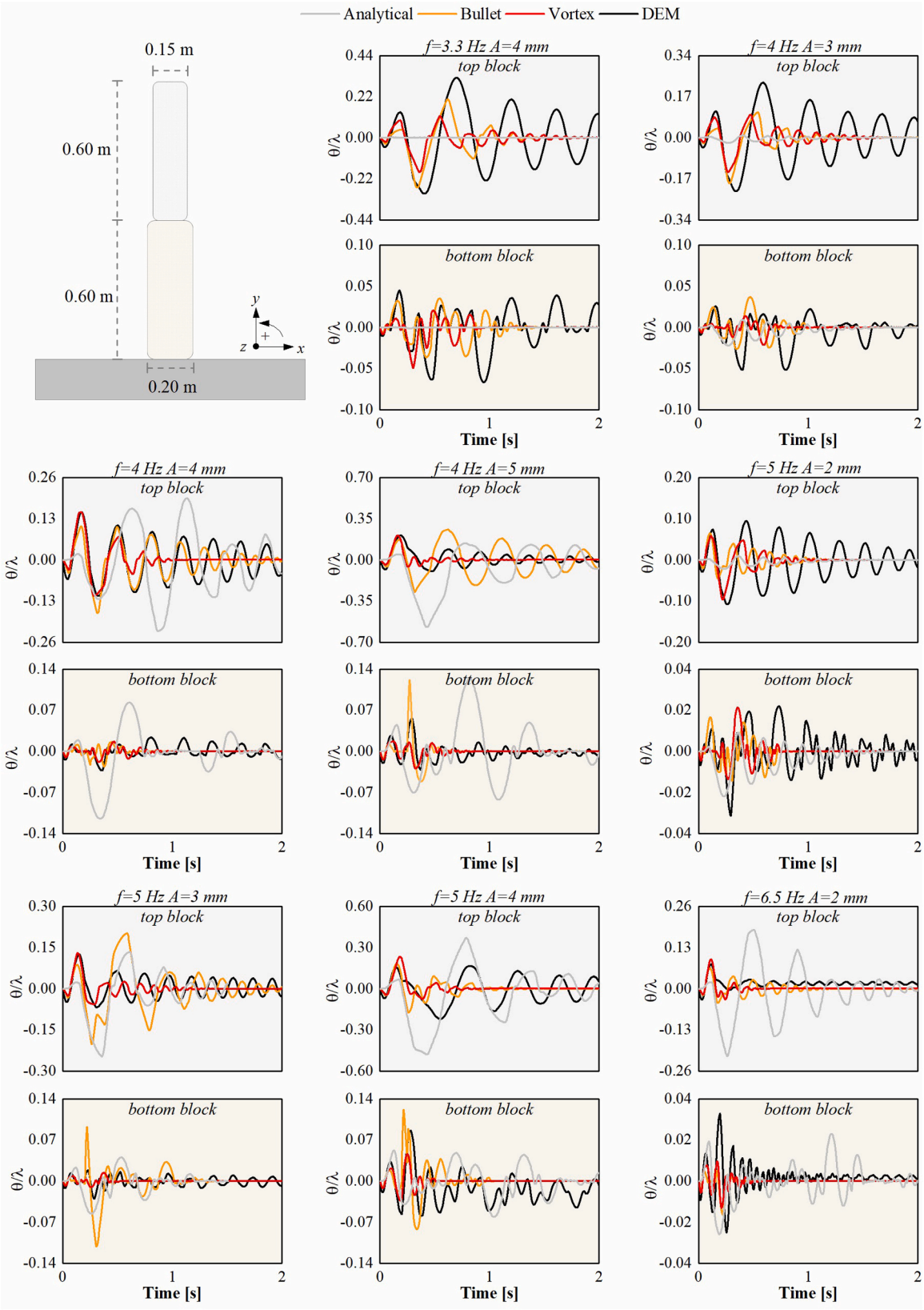

Fig. 12. Normalized rocking angle time-histories of two stacked blocks under sine-pulse excitations.

DEM failed to capture the maximum rocking angle at *5 Hz / 3 mm*, as the top block collapsed after one second. The ability of DEM to realistically simulate rocking motion may be attributed to its capacity to capture rotations not only about the primary axis but also about secondary axes, as previously observed in the sinusoidal response of single blocks. The physics engines show comparable maximum rocking angles, but their deviations from the experimental data are larger than those from DEM, ranging from −98 % to −26 % in Bullet and from −97 % to −31 % in

Table 9
Comparison of normalized maximum rocking angles obtained using analytical solutions, Bullet, Vortex and DEM, for the top block under sine-pulse excitations.

Frequency	Amplitude	Analytical	Bullet	Vortex	DEM
		$\frac{\theta_{an}}{\lambda}$	$\frac{\theta_{bl}}{\lambda}$	$\frac{\theta_{vx}}{\lambda}$	$\frac{\theta_{DEM}}{\lambda}$
[Hz]	[mm]	[-]	[-]	[-]	[-]
3.3	4	-	0.268	0.185	0.320
	3	0.022	0.190	0.142	0.227
4	4	0.225	0.168	0.151	0.151
	5	0.572	0.273	0.208	0.208
	2	0.022	0.065	0.096	0.108
5	3	0.247	0.203	0.131	0.125
	4	0.480	0.184	0.234	0.221
6.5	2	0.213	0.065	0.094	0.077

Table 10
Comparison of normalized maximum rocking angles obtained using analytical solutions, Bullet, Vortex and DEM, for the bottom block under sine-pulse excitations.

Frequency	Amplitude	Analytical	Bullet	Vortex	DEM
		$\frac{\theta_{an}}{\lambda}$	$\frac{\theta_{bl}}{\lambda}$	$\frac{\theta_{vx}}{\lambda}$	$\frac{\theta_{DEM}}{\lambda}$
[Hz]	[mm]	[-]	[-]	[-]	[-]
3.3	4	-	0.036	0.049	0.067
	3	0.022	0.037	0.021	0.052
4	4	0.114	0.026	0.018	0.033
	5	0.125	0.121	0.029	0.056
	2	0.022	0.017	0.021	0.031
5	3	0.055	0.111	0.014	0.030
	4	0.061	0.122	0.046	0.086
6.5	2	0.026	0.016	0.013	0.025

Vortex. The largest differences— −98 % for Bullet and −97 % for Vortex—occur when the software programs fail to detect experimental collapses. A similar situation is observed with the analytical solution, where the maximum rocking angles deviate by −86 % to −6 %, with the largest difference (-86 %) corresponding to undetected experimental collapses. As observed for the sine-pulse excitations, the initial rocking angles of the top block are nearly identical across Bullet, Vortex, and DEM, except for *5.0 Hz / 2 mm*, where DEM produced lower rocking angles. The analytical results show smaller rocking angles. In general, rocking angles using DEM stabilize more slowly than those from the other programs.

For the bottom blocks, the physics engines always underestimate maximum rocking angles, with percentage differences of 98 %-53 % for Bullet and 96 %-67 % for Vortex. Instead, the DEM models and the analytical solution in some cases overestimated and other cases underestimated them.

Note that the Peña et al. [62] themselves concluded that in the specific case of two stacked block specimens, tests were hardly repeatable. This can be observed when the dynamic response of complex rocking systems is investigated either experimentally [6] or numerically [5,60,85]. Hence, large deviations from measured values should not surprise the reader. Differences observed between prediction and test results shall not be directly used to quantify accuracy here. Of certain interest is, however, the fact that Bullet, Vortex and DEM generally yield comparable results.

The graphical representation of the normalized rocking angles versus the normalized acceleration (Fig. 15) shows that, for the top block, all numerical models follow the experimental trend up to a normalized acceleration of 1.48. Beyond this point, only the DEM model continues to match the experimental response, although it begins to predict overturning slightly earlier. Overall, the analytical solution tends to underpredict the top block's rotations, except at intermediate accelerations (1.45 and 1.74), where it aligns well with the experimental data. In contrast, neither the numerical models nor the analytical solution can simulate the experimentally measured rocking angles for the bottom block.

It is acknowledged that further work is required to fully evaluate performance of physics engines up to rocking-induced collapse, since some of the macro-blocks analyzed herein did not fail under the applied dynamic motion. This is partly investigated in some of our other recent work [83] focusing on the capabilities of physics engines (Bullet) in reproducing experimental and DEM out-of-plane failures of dry-joint meso-scale masonry assemblies. The results obtained in the above-mentioned research shows when the collapse is induced quasi-statically using a tilting platform, slightly conservative yet satisfactorily predictions can be achieved.

7. Conclusions

Physics engines are numerical tools conceived for visually plausible and expedited simulations of mechanical phenomena, including the dynamics of rigid particles, and are often used in movies, videogames

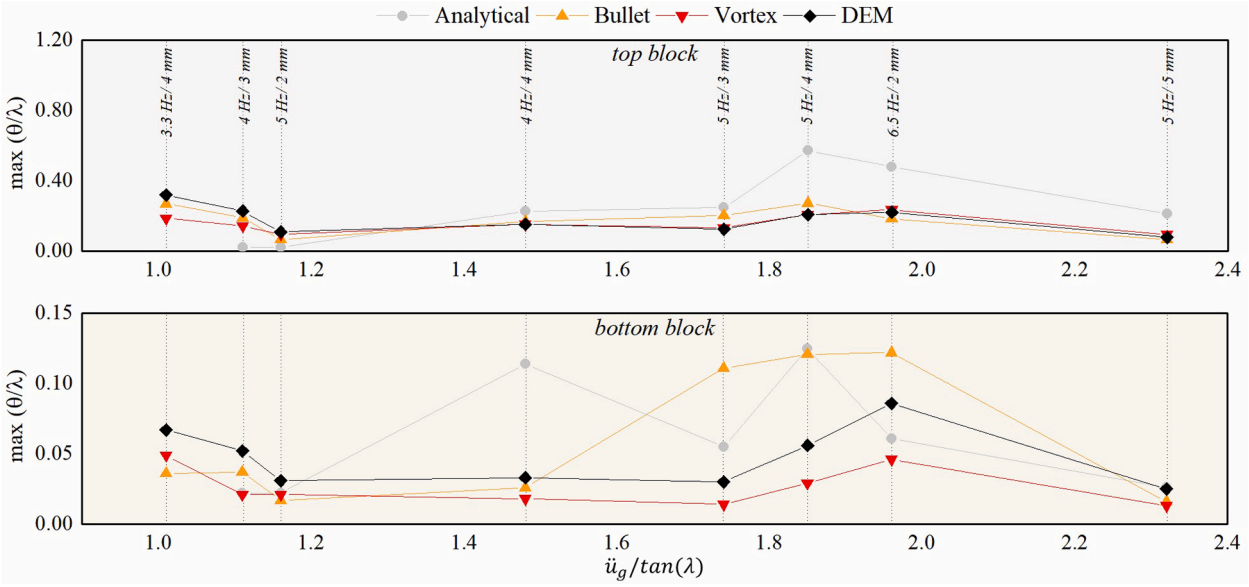

Fig. 13. Trends in the normalized maximum rocking angles of the stacked block model under sine-pulse excitation, as a function of normalized input acceleration.

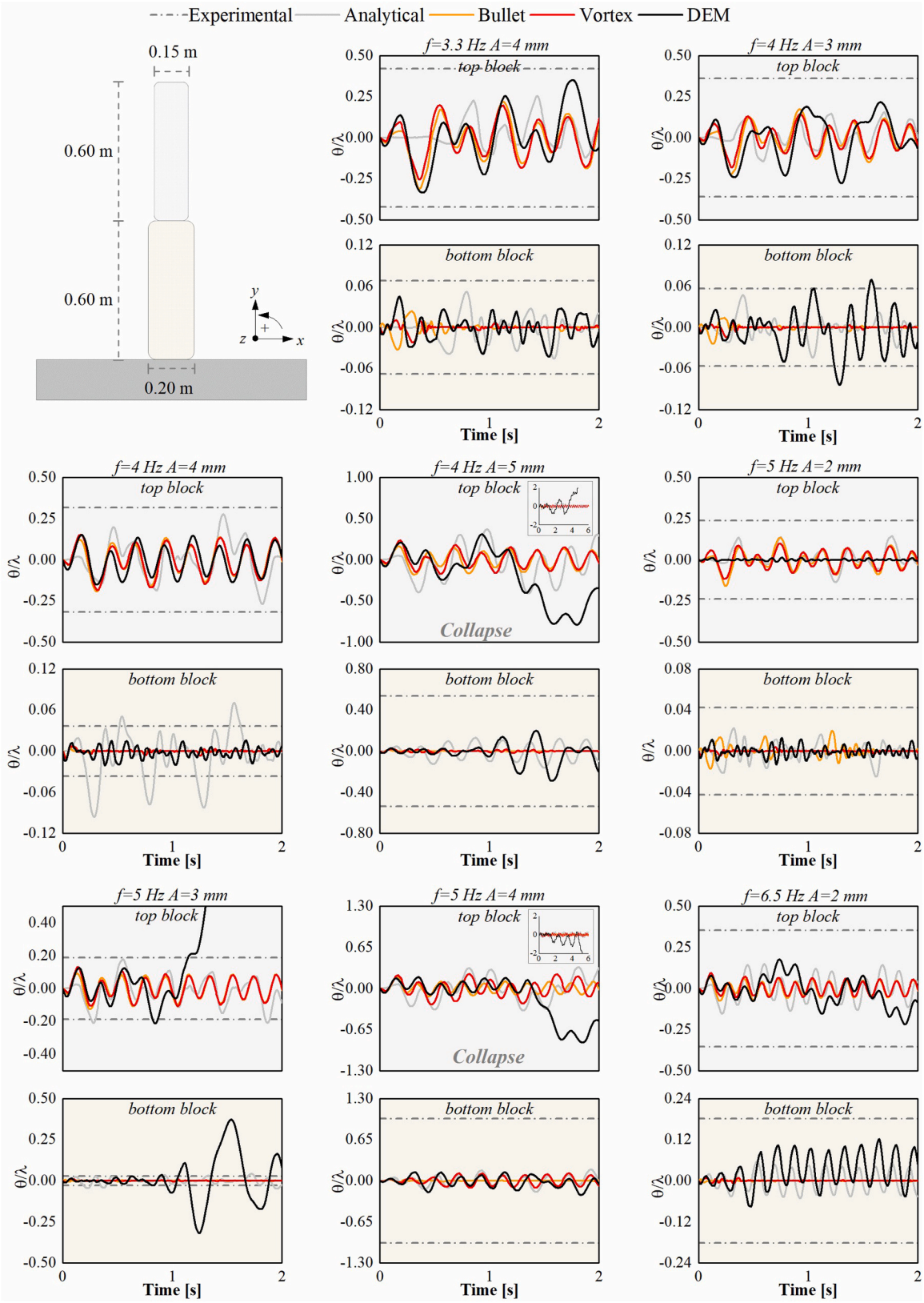

Fig. 14. Normalized rocking angle time-histories of two stacked blocks under sinusoidal excitations.

and virtual reality applications for creating digital animations. Conceptually, they present similarities with more rigorous yet computationally intensive discontinuum solvers leveraged by structural and earthquake engineers for assessing the rocking motion of blocky systems, including those made of highly vulnerable unreinforced masonry (URM).

This study is the first quantitative evaluation of two widely used physics engines, Bullet Physics (implemented in Blender, open-source)

Table 11
Percentage errors in maximum rocking angles obtained using analytical solutions, Bullet, Vortex and DEM, relative to experimental values for the top block under sinusoidal excitation (red indicates overestimations, blue underestimations vs experimental results).

	Analytical	Bullet	Vortex	DEM
	$\frac{\theta_{an}-\theta_{ex}}{\theta_{ex}}$	$\frac{\theta-\theta_{ex}}{\theta_{ex}}$	$\frac{\theta_{vx}-\theta_{ex}}{\theta_{ex}}$	$\frac{\theta_{DEM}-\theta_{ex}}{\theta_{ex}}$
f= 3.3 A= 4 mm	79 %	26 %	39 %	15 %
f= 4.0 A= 3 mm	44 %	38 %	46 %	9 %
f= 4.0 A= 4 mm	8 %	39 %	42 %	43 %
f= 4.0 A= 5 mm	96 %	98 %	97 %	collapsed
f= 5.0 A= 2 mm	26 %	33 %	38 %	28 %
f= 5.0 A= 3 mm	26 %	34 %	31 %	collapsed
f= 5.0 A= 4 mm	96 %	98 %	97 %	collapsed
f= 6.5 A= 2 mm	56 %	79 %	73 %	32 %

Table 12
Percentage errors in maximum rocking angles obtained using analytical solutions, Bullet, Vortex and DEM, relative to experimental values for the bottom block under sinusoidal excitation (red indicates overestimations, blue underestimations vs experimental results).

	Analytical	Bullet	Vortex	DEM
	$\frac{\theta_{an}-\theta_{ex}}{\theta_{ex}}$	$\frac{\theta_{bl}-\theta_{ex}}{\theta_{ex}}$	$\frac{\theta_{vx}-\theta_{ex}}{\theta_{ex}}$	$\frac{\theta_{DEM}-\theta_{ex}}{\theta_{ex}}$
f= 3.3 A= 4 mm	-	55 %	67 %	19 %
f= 4.0 A= 3 mm	253 %	57 %	74 %	91 %
f= 4.0 A= 4 mm	422 %	76 %	72 %	42 %
f= 4.0 A= 5 mm	70 %	98 %	96 %	35 %
f= 5.0 A= 2 mm	4 %	53 %	90 %	306 %
f= 5.0 A= 3 mm	242 %	78 %	70 %	1856 %
f= 5.0 A= 4 mm	82 %	98 %	88 %	49 %
f= 6.5 A= 2 mm	69 %	97 %	95 %	8 %

and Vortex (developed by CM Labs, commercial code), in simulating complex rocking phenomena of isolated and stacked rigid blocks under either free or forced motion. Various block aspect ratios, shapes, and boundary conditions were considered, and outcomes validated against experimental data, analytical predictions, and numerical simulations via 3DEC, a reference Distinct Element Method (DEM) software for the rigorous rocking analysis of URM. Key findings are summarized as follows:

- Both Bullet and Vortex can accurately simulate the free rocking of single rigid blocks with varying slenderness and initial rocking angles, yielding maximum errors on the order of 10^{-4} relative to the widely accepted Housner's analytical solution.
- Under sine-pulse forced rocking, both physics engines and DEM exhibited a maximum difference up to approximately ±20 % in predicted rocking angles compared to the analytical solution. In these cases, the physics engines produced an overdamped response, while DEM exhibited an underdamped behaviour attributable to its stiffness-damping approach.
- Under sinusoidal excitations, the maximum rocking angles produced by both physics engines and DEM were within + 12 % of the experimental values, whereas the analytical solution underestimated these angles by about 40 %. This discrepancy arises because the analytical model applies the input loads directly at the centroids of the blocks, whereas the numerical models apply them to the foundation blocks.
- For two stacked blocks under sine-pulse forced rocking, the initial rocking angles of the top block were similar between the physics engines and DEM, with average absolute errors of 26 % (Bullet) and 15 % (Vortex). However, larger discrepancies were observed for the bottom block, with absolute average errors of 76 % for Bullet and 45 % for Vortex.
- In the case of sinusoidal forced rocking for two-stacked blocks, both physics engines underestimated the maximum rocking angles when compared with experimental data: the top block's angles were underestimated by an average of 56 % in Vortex and 58 % in Bullet, while the bottom block's angles were underestimated by 77 % and 82 %, respectively. Notably, DEM provided more accurate predictions for the top block (with an absolute average error of 18 %) and was the only method capable of simulating the collapse of the top block under certain loads.
- The computational times for Bullet and Vortex were comparable and significantly lower than those for DEM. For instance, in the case of a single block subjected to a *5 Hz / 6 mm* excitation, Bullet and Vortex required approximately 150 s for the sine-pulse input and 53 s for the sinusoidal input, whereas the DEM simulations took 1440 and 1560 s, respectively. Similarly, for the analysis of two stacked blocks under a *5 Hz / 4 mm* excitation, Bullet and Vortex simulations required 489 s for the sine-pulse and 358 s for the sinusoidal input. In contrast, DEM simulations for the same scenarios required 7220 and 18055 seconds, respectively. It is important to note that DEM

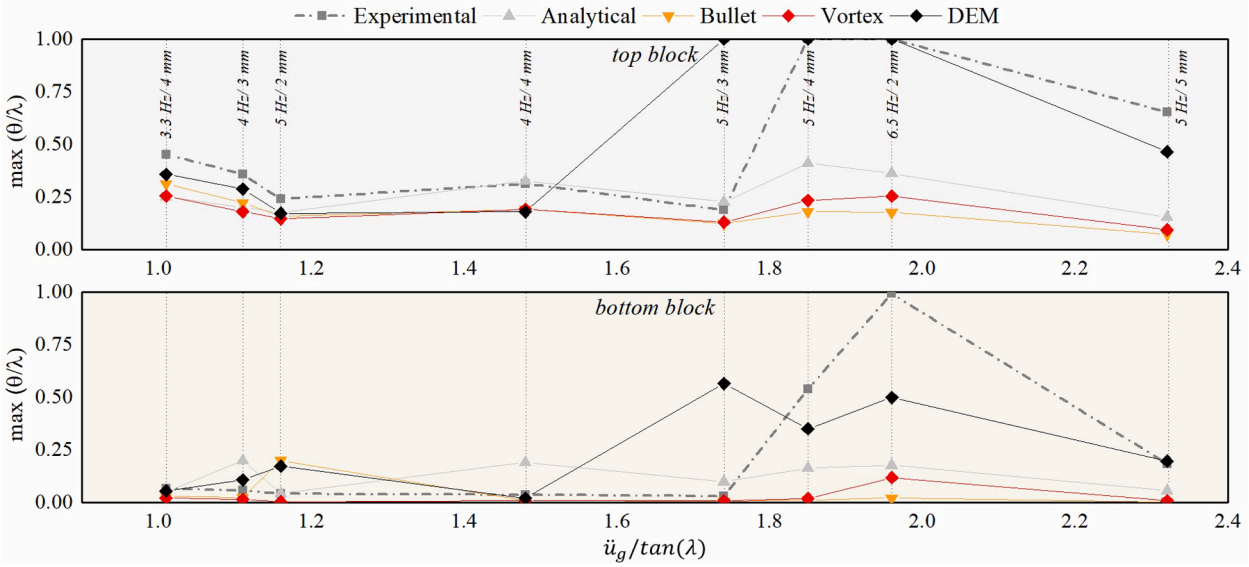

Fig. 15. Trends in the normalized maximum rocking angles of the stacked model under sinusoidal excitation, as a function of normalized input acceleration.

analyses were conducted on a high-performance workstation equipped with a 12th Gen Intel® Core™ i9–12900K processor (3.2 GHz) and 128 GB of RAM. In comparison, Bullet and Vortex simulations were carried out on a significantly less powerful machine, equipped with a 13th Gen Intel® Core™ i7–13700K processor (2.1 GHz) and 16 GB of RAM.

This study demonstrates that Bullet and Vortex can be used for the rocking analysis of rigid blocks and that their performance does not differ significantly from that of established DEM models (3DEC in this case). Because the analysis time required by physics engines is significantly lower than that of DEM, our results will enable researchers and engineers working within and beyond structural engineering to conduct larger-scale computations much more effectively, potentially involving complex configurations of isolated or stacked blocks. Future research will comparatively assess the capabilities of physics engines and DEM in simulating the dynamic response of multi-block dry-joint systems, also up to collapse, as well as the development of more advanced bonded particle models for physics engines.

CRediT authorship contribution statement

E. Giordano: Conceptualization, Methodology, Investigation, Validation, Formal analysis, Data curation, Writing – original draft, Writing – review & editing. **Y. Han:** Validation, Formal analysis, Data curation. **A. Wang:** Conceptualization, Visualization, Writing – original draft, Writing – review & editing. **G. Destro Bisol:** Conceptualization, Methodology, Investigation, Validation, Writing – original draft, Writing – review & editing. **S. Andrews:** Methodology, Investigation, Writing – original draft, Writing – review & editing, Supervision. **D. Malomo:** Conceptualization, Methodology, Investigation, Writing – original draft, Writing – review & editing, Supervision, Project administration, Funding acquisition.

Author contributions

All authors contributed to the study conception and design. The first draft of the manuscript was written by **E. Giordano**, **Y. Han**, **A. Wang** and **G. Destro Bisol,** and **D. Malomo** and S. **Andrews** review and editing the final draft. All authors read and approved the final manuscript. D. Malomo secured funding and co-directed the research with S. Andrews.

Funding

The authors declare that no funds, grants, or other support were received during the preparation of this manuscript.

Declaration of Competing Interest

The authors declare that they have no known competing financial interests or personal relationships that could have appeared to influence the work reported in this paper.

The author is an Editorial Board Member/Editor-in-Chief/Associate Editor/Guest Editor for this journal and was not involved in the editorial review or the decision to publish this article.

Acknowledgements

The authors acknowledge funding from the Government of Canada's New Frontiers in Research Fund (NFRF) [Ref. No. NFRFE-2022-00312]. Y. Han has received funding through the Centre d'études interuniversitaire des structures sous charges extrêmes (CEISCE), a strategic cluster supported by the Fonds de recherche du Québec - Nature et technologies (FRQ-NT). The authors thank CM Labs for kindly providing free access and support to/for Vortex Studio. Finally, the authors would like to thank Prof. Pulatsu (Carleton University) for sharing his valuable insights on fundamental differences and similarities between DEM and physics engines.

Data availability

The datasets presented in this study are available from the corresponding author on reasonable request.

References

[1] Acikgoz S, Dejong MJ. The interaction of elasticity and rocking in flexible structures allowed to uplift. Earthq Eng Struct Dyn 2012;41:2177–94. https://doi.org/10.1002/eqe.2181.
[2] Aghagholizadeh M. A finite element model for seismic response analysis of vertically-damped rocking-columns. Eng Struct 2020;219:447–66. https://doi.org/10.1016/j.engstruct.2020.110894.
[3] Andrews S., Erleben K., Ferguson Z. (2022) Contact and friction simulation for computer graphics.
[4] Anitescu M, Potra FA. Formulating dynamic Multi-Rigid-Body contact problems with friction as solvable linear complementarity problems. Nonlinear Dyn 1997;14:231–47. https://doi.org/10.1023/A:1008292328909.
[5] Aslam M, Godden WG, Scalise DT. Earthquake rocking response of rigid bodies. J Struct Div 1980;106:377–92. https://doi.org/10.1061/JSDEAG.0005363.
[6] Bachmann JA, Strand M, Vassiliou MF, et al. Is rocking motion predictable. Earthq Eng Struct Dyn 2018;47:535–52. https://doi.org/10.1002/eqe.2978.
[7] Baraff D. (1994) Fast contact force computation for nonpenetrating rigid bodies. In: Proceedings of the 21st Annual Conference on Computer Graphics and Interactive Techniques, SIGGRAPH 1994. Association for Computing Machinery, New York, NY, USA, pp 23–34.
[8] Baumgarte J. Stabilization of constraints and integrals of motion in dynamical systems. Comput Methods Appl Mech Eng 1972;1:1–16. https://doi.org/10.1016/0045-7825(72)90018-7.
[9] Beatini V, Royer-Carfagni G, Tasora A. A regularized non-smooth contact dynamics approach for architectural masonry structures. Comput Struct 2017;187:88–100. https://doi.org/10.1016/j.compstruc.2017.02.002.
[10] Berton J.A., Chuang K.-L. (2016) Effects of Very High Frame Rate Display in Narrative CGI Animation. In: 2016 20th International Conference Information Visualisation (IV). pp 395–398.
[11] Chatzis MN, García Espinosa M, Needham C, Williams MS. Energy loss in systems of stacked rocking bodies. J Eng Mech 2018;144:4018044. https://doi.org/10.1061/(asce)em.1943-7889.0001443.
[12] CM Labs Simulations (2024) Vortex Studio.
[13] Coumans E. (2015) Bullet physics simulation. In: ACM SIGGRAPH 2015 Courses. p 1.
[14] Courant R, Friedrichs K, Lewy H. On the partial difference equations of mathematical physics. IBM J Res Dev 1967;11:215–34. https://doi.org/10.1147/rd.112.0215.
[15] Cundall PA. The measurement and analysis of accelerations in rock slopes. Ph d thesis. Imp Coll; 1971.
[16] Cundall P.A. (1971a) A computer model for simulating progressive large-scale movements in blocky rock systems. In: In Proceedings of the Symposium of the International Society of Rock Mechanics. p No. 8.
[17] Cundall PA. Formulation of a three-dimensional distinct element model-Part I. A scheme to detect and represent contacts in a system composed of many polyhedral blocks. Int J Rock Mech Min Sci 1988;25:107–16. https://doi.org/10.1016/0148-9062(88)92293-0.
[18] Cundall PA, Strack ODL. A discrete numerical model for granular assemblies. Géotechnique 1979;29:47–65. https://doi.org/10.1680/geot.1979.29.1.47.
[19] DeJong MJ. Seismic assessment strategies for masonry structures. Phd thesis. Massachusetts Inst Technol United States; 2009.
[20] DeJong M.J., Dimitrakopoulos E.G. (2012) Equivalent rocking systems: fundamental rocking parameters. In: 15WCEE. Lisbon, Portugal, pp 1–10.
[21] DeJong MJ, Vibert C. Seismic response of stone masonry spires: computational and experimental modeling. Eng Struct 2012;40:566–74.
[22] Destro Bisol G, DeJong M, Liberatore D, Sorrentino L. Analysis of seismically-isolated two-block systems using a multi–rocking-body dynamic model. Comput Civ Infrastruct Eng 2023;38:1583–604. https://doi.org/10.1111/mice.13012.
[23] Destro Bisol G, Prajapati S, Sorrentino L, AlShawa O. Vertical spanning wall elastically restrained at the top: validation and parametric dynamic analysis. Bull Earthq Eng 2024;22:3951–78. https://doi.org/10.1007/s10518-024-01909-w.
[24] Enzenhöfer A, Andrews S, Teichmann M, Kövecses J. Comparison of mixed linear complementarity problem solvers for multibody simulations with contact. In: Andrews S, Erleben K, Jaillet F, Zachmann G, editors. Workshop on Virtual Reality Interaction and Physical Simulation. The Eurographics Association; 2018.
[25] Fang Y, Li M, Cao Y, et al. Augmented incremental potential contact for sticky interactions. IEEE Trans Vis Comput Graph 2024;30:5596–608. https://doi.org/10.1109/TVCG.2023.3295656.
[26] Ferrante A, Giordano E, Clementi F, et al. FE vs. De modeling for the nonlinear dynamics of a historic church in central Italy. Geosciences 2021;11:189. https://doi.org/10.3390/geosciences11050189.

[27] Galvez F, Sorrentino L, Dizhur D, Ingham JM. Damping considerations for rocking block dynamics using the discrete element method. Earthq Eng Struct Dyn 2022; 51:935–57. https://doi.org/10.1002/eqe.3598.

[28] Galvez F, Sorrentino L, Dizhur D, Ingham JM. Seismic rocking simulation of unreinforced masonry parapets and façades using the discrete element method. Earthq Eng Struct Dyn 2022;51:1840–56. https://doi.org/10.1002/eqe.3641.

[29] Gobbin F, de Felice G, Lemos JV. Numerical procedures for the analysis of collapse mechanisms of masonry structures using discrete element modelling. Eng Struct 2021;246:113047. https://doi.org/10.1016/j.engstruct.2021.113047.

[30] Godio M, Beyer K. Evaluation of force-based and displacement-based out-of-plane seismic assessment methods for unreinforced masonry walls through refined model simulations. Earthq Eng Struct Dyn 2019;48:454–75. https://doi.org/10.1002/eqe.3144.

[31] Goldstein H., Poole C., Safko J. (1980) Classical mechanics addison-wesley.

[32] Hart R, Cundall PA, Lemos J. Formulation of a three-dimensional distinct element model-Part II. Mechanical calculations for motion and interaction of a system composed of many polyhedral blocks. Int J Rock Mech Min Sci 1988;25:117–25. https://doi.org/10.1016/0148-9062(88)92294-2.

[33] He H, Zheng J. Simulations of realistic granular soils in oedometer tests using physics engine. Int J Numer Anal Methods Geomech 2020;44:983–1002. https://doi.org/10.1002/nag.3031.

[34] Hochbruck M, Lubich C, McLachlan R, Sanz-Serna JM. Geometric numerical integration. Oberwolfach Rep 2022;18:943–99. https://doi.org/10.4171/owr/2021/17.

[35] Housner GW. The behavior of inverted pendulum structures during earthquakes. Bull Seismol Soc Am 1963;53:403–17. https://doi.org/10.1785/BSSA0530020403.

[36] Itasca Consulting Group I (2016) 3DEC—theory and background.

[37] Izadi E, Bezuijen A. Simulating direct shear tests with the bullet physics library: a validation study. PLoS One 2018;13:e0195073. https://doi.org/10.1371/journal.pone.0195073.

[38] Jing L., Stephansson O. (2007) Explicit Discrete Element Method for Block Systems - the Distinct Element Method. In: Jing L, Stephansson OBT-D in GE (eds) Developments in Geotechnical Engineering. Elsevier, pp 235–316.

[39] Komaragiri S, Gigliotti A, Bhasin A. Feasibility of using a physics engine to virtually compact asphalt mixtures in a gyratory compactor. Constr Build Mater 2021;308: 124977. https://doi.org/10.1016/j.conbuildmat.2021.124977.

[40] Kovacs MA, Wiebe L. Controlled rocking CLT walls for buildings in regions of moderate seismicity: design procedure and numerical collapse assessment. J Earthq Eng 2019;23:750–70. https://doi.org/10.1080/13632469.2017.1326421.

[41] Lacoursiere C. A regularized time stepper for multibody systems. Department of Computing Science, Umeå University; 2006.

[42] Lagomarsino S. Seismic assessment of rocking masonry structures. Bull Earthq Eng 2015;13:97–128. https://doi.org/10.1007/s10518-014-9609-x.

[43] Lemos JV. Discrete element modeling of masonry structures. Int J Arch Herit 2007; 1:190–213.

[44] Lemos JV. Discrete element modeling of the seismic behavior of masonry construction. Buildings 2019;9:43. https://doi.org/10.3390/buildings9020043.

[45] Lemos JV, Oliveira CS, Navarro M. 3-D nonlinear behavior of an obelisk subjected to the lorca May 11, 2011 strong motion record. Eng Fail Anal 2015;58:212–28. https://doi.org/10.1016/j.engfailanal.2015.09.001.

[46] Lemos JV, Sarhosis V. Dynamic analysis of masonry arches using Maxwell damping. Structures 2023;49:583–92. https://doi.org/10.1016/j.istruc.2023.01.139.

[47] Lloyd J.E. (2005) Fast implementation of Lemke's algorithm for rigid body contact simulation. In: Proceedings - IEEE International Conference on Robotics and Automation. pp 4538–4543.

[48] Lorenzis LDe, DeJong M, Ochsendorf J. Failure of masonry arches under impulse base motion. Earthq Eng Struct Dyn 2007;36:2119–36. https://doi.org/10.1002/eqe.719.

[49] Ma Q.T., Parshottam S., Montalla M. (2018) Modelling rocking behaviour using physics engine simulation. In: 11th National Conference on Earthquake Engineering 2018, NCEE 2018: Integrating Science, Engineering, and Policy. pp 1212–1222.

[50] Macklin M., Storey K., Lu M., et al (2019) Small steps in physics simulation. In: Proceedings - SCA 2019: ACM SIGGRAPH / Eurographics Symposium on Computer Animation. Association for Computing Machinery, Inc.

[51] Malomo D, DeJong MJ. A Macro-Distinct element model (M-DEM) for out-of-plane analysis of unreinforced masonry structures. Eng Struct 2021;244. https://doi.org/10.1016/j.engstruct.2021.112754.

[52] Malomo D, Mehrotra A, DeJong MJ. Distinct element modeling of the dynamic response of a rocking podium tested on a shake table. Earthq Eng Struct Dyn 2021; 50:1469–75. https://doi.org/10.1002/eqe.3404.

[53] Malomo D, Pinho R, Penna A. Applied element modelling of the dynamic response of a Full-Scale clay brick masonry building specimen with flexible diaphragms. Int J Arch Herit 2020;14:1484–501. https://doi.org/10.1080/15583058.2019.1616004.

[54] Malomo D., Pulatsu B. (2024) Discontinuum models for the structural and seismic assessment of unreinforced masonry structures: a critical appraisal. In: Structures. p 106108.

[55] Mehrotra A, DeJong M. The performance of slender monuments during the 2015 gorkha, Nepal, earthquake. Earthq Spectra 2017;33:S321–43. https://doi.org/10.1193/120616EQS223M.

[56] Milaszewicz JP. Improving jacobi and Gauss-Seidel iterations. Linear Algebra Appl 1987;93:161–70. https://doi.org/10.1016/S0024-3795(87)90321-1.

[57] Mizutani WK, Daros VK, Kon F. Software architecture for digital game mechanics: a systematic literature review. Entertain Comput 2021;38:100421. https://doi.org/10.1016/j.entcom.2021.100421.

[58] Moioli G. Introducing Blender 3.0." *Introduction to Blender 3.0: Learn Organic and Architectural Modeling, Lighting, Materials, Painting, Rendering, and Compositing with Blender*. Berkeley, CA: Apress; 2022. p. 1–63.

[59] Oktiovan YP, Davis L, Wilson R, et al. Simplified Micro-Modeling of a masonry Cross-Vault for seismic assessment using the distinct element method. Int J Arch Herit 2023;00:1–34. https://doi.org/10.1080/15583058.2023.2277328.

[60] Papantonopoulos C, Psycharis IN, Papastamatiou DY, et al. Numerical prediction of the earthquake response of classical columns using the distinct element method. Earthq Eng Struct Dyn 2002;31:1699–717. https://doi.org/10.1002/eqe.185.

[61] Papastamatiou D, Psycharis L. Seismic response of classical monuments-a numerical perspective developed at the temple of apollo in bassae, Greece. Terra Nov 1993;5:591–601. https://doi.org/10.1111/j.1365-3121.1993.tb00309.x.

[62] Peña F, Lourenço PB, Campos-Costa A. Experimental dynamic behavior of free-standing multi-block structures under seismic loadings. J Earthq Eng 2008;12: 953–79. https://doi.org/10.1080/13632460801890513.

[63] Peña F, Prieto F, Lourenço PB, et al. On the dynamics of rocking motion of single rigid-block structures. Earthq Eng Struct Dyn 2007;36:2383–99. https://doi.org/10.1002/eqe.739.

[64] Prajapati S, Destro Bisol G, AlShawa O, Sorrentino L. Non-linear dynamic model of a two-bodies vertical spanning wall elastically restrained at the top. Earthq Eng Struct Dyn 2022;51:2627–47. https://doi.org/10.1002/eqe.3692.

[65] Psycharis IN. Dynamic behaviour of rocking two-block assemblies. Earthq Eng Struct Dyn 1990;19:555–75. https://doi.org/10.1002/eqe.4290190407.

[66] Pulatsu B. Coupled elasto-softening contact models in DEM to predict the in-plane response of masonry walls. Comput Part Mech 2023:1–12. https://doi.org/10.1007/s40571-023-00586-x.

[67] Pulatsu B, Bretas EM, Lourenço PB. Discrete element modeling of masonry structures: validation and application. Earthq Struct 2016;11:563–82. https://doi.org/10.12989/eas.2016.11.4.563.

[68] Pulatsu B, Erdogmus E, Lourenco P, et al. Discontinuum analysis of the fracture mechanism in masonry prisms and wallettes via discrete element method. Meccanica 2020;55. https://doi.org/10.1007/s11012-020-01133-1.

[69] Rajath S, Shivakumar ND, Pradhan KS. Rovers with Rocker-Bogie mechanisms: a review of progress and innovations in design, manufacturing, and control. Proc Inst Mech Eng Part C J Mech Eng Sci 2024;238:6560–83. https://doi.org/10.1177/09544062231224541.

[70] Reggiani Manzo N, Vassiliou MF. Displacement-based analysis and design of rocking structures. Earthq Eng Struct Dyn 2019;48:1613–29. https://doi.org/10.1002/eqe.3217.

[71] Sarti F, Palermo A, Pampanin S. Development and testing of an alternative dissipative posttensioned rocking timber wall with boundary columns. J Struct Eng 2016;142:E4015011. https://doi.org/10.1061/(asce)st.1943-541x.0001390.

[72] Scattarreggia N, Malomo D, DeJong M. A new distinct element meso-model for simulating the rocking-dominated seismic response of RC columns. Earthq Eng Struct Dyn 2022;52. https://doi.org/10.1002/eqe.3782.

[73] Schiavoni M, Giordano E, Roscini F, Clementi F. Advanced numerical insights for an effective seismic assessment of historical masonry aggregates. Eng Struct 2023; 285:115997. https://doi.org/10.1016/j.engstruct.2023.115997.

[74] Silcowitz M, Niebe S, Erleben K. Interactive rigid body dynamics using a projected gauss-seidel subspace minimization method. In: Richard P, Braz J, editors. Communications in Computer and Information Science, 229. Berlin, Heidelberg: Springer Berlin Heidelberg; 2011. p. 218.

[75] So E, Spence R. Estimating shaking-induced casualties and building damage for global earthquake events: a proposed modelling approach. Bull Earthq Eng 2013; 11:347–63. https://doi.org/10.1007/s10518-012-9373-8.

[76] Sorrentino L, AlShawa O, Decanini LD. The relevance of energy damping in unreinforced masonry rocking mechanisms. Experimental and analytic investigations. Bull Earthq Eng 2011;9:1617–42.

[77] Sorrentino L, Masiani R, Griffith MC. The vertical spanning strip wall as a coupled rocking rigid body assembly. Struct Eng Mech 2008;29:433–53. https://doi.org/10.12989/sem.2008.29.4.433.

[78] Spanos PD, Roussis PC, Politis NPA. Dynamic analysis of stacked rigid blocks. Soil Dyn Earthq Eng 2001;21:559–78. https://doi.org/10.1016/S0267-7261(01)00038-0.

[79] Stewart DE, Trinkle JC. An implicit time-stepping scheme for rigid body dynamics with inelastic collisions and Coulomb friction. Int J Numer Methods Eng 1996;39: 2673–91. https://doi.org/10.1002/(SICI)1097-0207(19960815)39:15<2673::AID-NME972>3.0.CO;2-I.

[80] Tabbara M, Karam G, Jello J, Beaino C. Rocking, wobbling and overturning of the multidrum columns of baalbek under periodic pulses. J Seismol 2021;25:1209–26. https://doi.org/10.1007/s10950-021-10023-2.

[81] The MathWorks Inc (2024) MATLAB version: R2024b.

[82] Wagner W.J. (2025) Deriving The Fundamental Equation of Earthmoving and Configuring Vortex Studio Earthmoving Simulation for Soil Property Estimation Experimentation. arXiv Prepr arXiv250519330.

[83] Wang A, Pulatsu B, Andrews S, Malomo D. Breaking boundaries: discontinuum failure analysis of dry-joint masonry using physics engine models. Eng Struct 2025; 342:120916. https://doi.org/10.1016/j.engstruct.2025.120916.
[84] Wilson R, Szabó S, Funari MF, et al. A comparative computational investigation on the In-Plane behavior and capacity of Dry-Joint URM walls. Int J Arch Herit 2024; 18:849–70. https://doi.org/10.1080/15583058.2023.2209776.
[85] Yim C, Chopra AK, Penzien J. Rocking response of rigid blocks to earthquakes. Earthq Eng Struct Dyn 1980;8:565–87. https://doi.org/10.1002/eqe.4290080606.
[86] Zhang J, Makris N. Rocking response of Free-Standing blocks under cycloidal pulses. J Eng Mech 2001;127:473–83. https://doi.org/10.1061/(ASCE)0733-9399(2001)127:5(473).
[87] Zhong C, Christopoulos C. Finite element analysis of the seismic shake-table response of a rocking podium structure. Earthq Eng Struct Dyn 2021;50:1223–30. https://doi.org/10.1002/eqe.3397.